

# An improved fringe-region technique for the representation of gravity waves in large-eddy simulation with application to wind farms

Luca Lanzilao · Johan Meyers

**Abstract** Large-eddy simulations of the atmospheric boundary layer are often performed using pseudo-spectral methods, which adopt a fringe-region approach to introduce inflow boundary conditions. However, we notice that a standard fringe-region technique excites spurious gravity waves when stratified atmospheres are considered, therefore enhancing the amount of energy reflected from the top of the domain and perturbing the velocity and pressure fields downstream. In this work, we develop a new fringe-region method that imposes the inflow conditions while limiting spurious effects on the surrounding flow. This is achieved by locally damping the convective term in the vertical momentum equation. We first apply the standard and wave-free fringe-region techniques to two-dimensional inviscid-flow simulations subjected to 169 different atmospheric states. A similar study is performed on a three-dimensional domain using a couple of atmospheric states. In all cases, the new fringe-region technique outperforms the standard method, imposing the inflow conditions with a minimal impact on the surrounding flow. Moreover, we also investigate the performance of two already existing non-reflective upper boundary conditions, that is a Rayleigh damping layer (RDL) and a radiation condition (RC). Results highlight the importance of carefully tuning the RDL to limit the distortion of the numerical solution. Also, we find that the tuned RDL outperforms the RC in all cases. Finally, the tuned RDL together with the wave-free fringe-region method are applied to an LES of a wind farm operating in a conventionally neutral boundary layer, for which we measure a reflectivity of only 0.75%.

**Keywords** Fringe-region technique · Gravity waves · Large-eddy simulation · Wind-farm simulation

## 1 Introduction

The constant increase of computational resources has made large-eddy simulation (LES) studies one of the most popular tools for analyzing the atmospheric boundary layer (ABL) responses to wind-farm forcing (Porté-Agel et al., 2020). One of the key aspects that influences such dynamics is the thermal stratification. Offshore, the ABL is often characterized by a neutral boundary layer capped by an inversion layer and a stably stratified atmosphere aloft (Smedman et al., 1997). This type of ABL is often defined as a conventionally neutral boundary layer (CNBL) (Allaerts, 2016). In such conditions, the momentum sink generated by the farm in the lower part of the ABL pushes upward the capping inversion, which in turns triggers gravity waves that propagate energy through the free atmosphere. To date, this phenomenon has been only investigated numerically, often with pseudo-spectral solvers which adopt a fringe-region approach to introduce inflow boundary conditions (Stevens et al., 2014; Munters et al., 2016a; Allaerts and Meyers, 2017, 2018; Wu and Porté-Agel, 2017; Gadde and Stevens, 2021; Stieren et al., 2021). This technique adds a body force to the right-hand side of the momentum and temperature equations, penalizing the error between the actual flow field and the desired inflow in a region usually located at the end of the domain (Spalart and Watmuff, 1993; Lundbladh et al., 1999;

---

Luca Lanzilao · Johan Meyers  
 Department of Mechanical Engineering, KU Leuven, Celestijnenlaan 300A–Bus 2421, B3001  
 E-mail: luca.lanzilao@kuleuven.be

Nordstrom et al., 1999; Inoue et al., 2014). The desired inflow can be a simple unidirectional and laminar flow, or a fully developed turbulent velocity profile obtained with synthetic turbulence generators or with a concurrent precursor method (Stevens et al., 2014; Dhamankar et al., 2015; Munters et al., 2016b). As mentioned by Dhamankar et al. (2015), an ideal inflow boundary condition should not introduce any spurious artefacts in the numerical solution. However, the capping inversion height at the end of the domain differs from the one of the inflow condition since the farm forcing displaces upward the inversion layer and triggers trapped gravity waves (Nappo, 2002; Allaerts and Meyers, 2019). Hence, the body force applied within the fringe region inevitably modify the capping inversion height to restore the inflow conditions, thereby exciting spurious gravity waves and perturbing the velocity and pressure fields downstream. These waves are numerical artefacts which distort the flow fields in the domain of interest and enhance the amount of energy reflected from the top of the domain. The results presented by Allaerts and Meyers (2017, 2018) show the presence of such spurious gravity waves, although they are not discussed by the authors. A similar behaviour is also observed in the work of Wu and Porté-Agel (2017), which uses a different pseudo-spectral solver from the one adopted in this manuscript.

Wind-farm induced gravity waves absorb energy within the ABL, transporting it at higher altitudes (Smith, 2010, 2022; Wu and Porté-Agel, 2017; Allaerts and Meyers, 2017, 2018, 2019; Lanzilao and Meyers, 2021; Devesse et al., 2022; Maas and Raasch, 2022). The energy is then released when the waves break down (Nappo, 2002; Sutherland, 2010). In a real-case scenario (and in the absence of potential temperature gradient variations in the free atmosphere), the energy is only transported upward since the source is located at the ground level. However, the boundaries of the computational domain allow the waves to reflect back, introducing disturbances within the domain. To overcome this issue, Klemp and Lilly (1977) introduced a Rayleigh damping layer (RDL) at the top of the domain to damp out gravity waves before they would have reached the upper boundary. Since then, this technique has been used extensively in mountain-wave simulations (Klemp and Lilly, 1977; Durran and Klemp, 1983; Teixeira, 2014), mesoscale models (Klemp et al., 2018; Powers et al., 2017) and LES of large wind farms (Allaerts and Meyers, 2017; Wu and Porté-Agel, 2017; Allaerts and Meyers, 2018; Gadde and Stevens, 2021; Maas and Raasch, 2022). The efficiency of this sponge layer increases with its vertical dimension. Klemp and Lilly (1977) recommended that the vertical extent should be about  $3/2$  times the gravity-wave vertical wavelength, which ranges approximately between 1 and 10 km. Therefore, the RDL usually occupies a large part of the computational domain and as a result can be computationally expensive. This shortcoming was fixed by Béland and Warn (1975) and Bennett (1976), who proposed an upper boundary condition which allows to radiate energy out of the domain without the need of a sponge layer. However, their technique requires evaluation of Laplace transforms, leading to unacceptable storage requirements when time integration is performed over a large number of time steps. Klemp and Durran (1982) and Bougeault (1982) were the first ones to propose an exact and parameter-free radiation boundary condition for linear hydrostatic Boussinesq equations in the absence of the Coriolis force, which did not require the computation of Laplace transforms. Despite the numerous assumptions, this radiation condition (RC) has been successfully used in several mesoscale models (Jiang and Doyle, 2004; Doyle et al., 2005; Klemp et al., 2018). Finally, other studies have opted for both strategies, that is using a RDL in combination with a RC at the top of the domain (Taylor and Sarkar, 2007, 2008). We note that also a perfectly matched layer technique could be adopted to avoid wave reflection (Hu, 2008; Parrish and Hu, 2009). However, when this method is applied to Navier–Stokes equations, it results in a coupled system of more than twenty absorbing boundary equations, becoming too complex and computationally expensive (Hu et al., 2008). Therefore, we do not further consider this technique in the current manuscript.

The goal of this work is twofold. First, we develop a wave-free fringe-region technique by locally damping the convective term in the vertical momentum equation to limit the advection of fringe-induced gravity waves into the domain of interest. Second, we show the importance of properly tuning the RDL to minimize the amount of energy reflected from the top of the

domain. Moreover, we maximize its computational efficiency and we compare its performances against a RC.

The article is further organized as follows. The numerical aspects together with the upper boundary conditions and fringe-region techniques are described in Sect. 2. To tune and test the standard and wave-free fringe-region methods, the RDL and the RC, we use two- and three-dimensional inviscid-flow simulations. These results are discussed in Sects. 3 and 4, respectively. Subsequently, the methods are demonstrated in a LES of a wind farm in Sect. 5. Finally, conclusions are summarized in Sect. 6.

## 2 Methodology

### 2.1 Governing Equations

The simulations performed in this study are based on the incompressible filtered Navier–Stokes equations coupled with a transport equation for the potential temperature and read as

$$\frac{\partial \tilde{u}_i}{\partial x_i} = 0, \quad (1)$$

$$\frac{\partial \tilde{u}_i}{\partial t} + \frac{\partial}{\partial x_j} (\tilde{u}_j \tilde{u}_i) = 2f_c \epsilon_{ij3} \tilde{u}_j + \delta_{i3} g \frac{\tilde{\theta} - \theta_0}{\theta_0} - \frac{\partial \tau_{ij}^{sgs}}{\partial x_j} - \frac{1}{\rho_0} \frac{\partial \tilde{p}^*}{\partial x_i} - \frac{1}{\rho_0} \frac{\partial p_\infty}{\partial x_i} + f_i^{tot}, \quad (2)$$

$$\frac{\partial \tilde{\theta}}{\partial t} + \frac{\partial}{\partial x_j} (\tilde{u}_j \tilde{\theta}) = - \frac{\partial q_j^{sgs}}{\partial x_j}, \quad (3)$$

where the horizontal directions are denoted with  $i = 1, 2$  while the vertical one is indicated by  $i = 3$ . The filtered velocity and potential temperature fields are noted with  $\tilde{u}_i$  and  $\tilde{\theta}$ . The first term on the right-hand side represents the Coriolis force due to planetary rotation, where the frequency  $f_c$  depends on the Earth's latitude. Thermal buoyancy is taken into account by the second term, where  $g = 9.81 \text{ m s}^{-2}$  denotes the gravitational constant and  $\theta_0$  a reference temperature. Several orders of magnitude separate the smallest and largest scales in boundary-layer flows, therefore we omit the resolved effects of viscous momentum transfer and diffusive heat transfer. Instead, these effects are modelled by the subgrid-scale stress tensor  $\tau_{ij}^{sgs}$  and the subgrid-scale heat flux  $q_j^{sgs}$ . The filtered modified pressure, denoted with  $\tilde{p}^*$ , represents pressure fluctuations around a steady background pressure  $p_\infty$ , which is used to drive the flow across the domain. Note that the trace of the subgrid-scale stress tensor is absorbed into  $\tilde{p}^*$ . Finally, the term  $f_i^{tot} = f_i + f_i^{ra} + f_i^{fr}$  groups all external forces exerted on the flow. Here,  $f_i^{ra}$  and  $f_i^{fr}$  represent the body forces applied within the RDL and fringe region, respectively, while  $f_i$  denotes a generic force applied within the ABL, e.g. originating from wind turbines. The notation  $(x_1, x_2, x_3)$  and  $(x, y, z)$  together with  $(\tilde{u}_1, \tilde{u}_2, \tilde{u}_3)$  and  $(\tilde{u}, \tilde{v}, \tilde{w})$  are used interchangeably. Moreover, for sake of simplicity, the tilde will not be used in the rest of the manuscript.

The LES code SP-Wind is used to solve the governing equations (Calaf et al., 2010; Goit and Meyers, 2015; Allaerts and Meyers, 2017; Munters and Meyers, 2018; Allaerts and Meyers, 2018). The solver uses a Fourier pseudo-spectral method to discretize the streamwise ( $x$ ) and spanwise ( $y$ ) directions while for the vertical dimension ( $z$ ) a symmetry-preserving fourth-order finite difference scheme is adopted (Verstappen and Veldman, 2003). A classic fourth-order Runge–Kutta scheme is used for the temporal component, with a time step based on a Courant–Friedrichs–Lewy number of 0.4. A Smagorinsky type model proposed by Stevens et al. (2000) is used to account for the effects of subgrid-scale motions on the resolved flow. The Smagorinsky coefficient is set to  $C_s = 0.14$ , similarly to Calaf et al. (2010) and Allaerts and Meyers (2017). The wall damping function used by Mason and Thomson (1992) is adopted to damp  $C_s$  near the wall. The Poisson equation is solved during every stage of the Runge–Kutta scheme to enforce continuity. The constant pressure gradient which drives the flow through the domain is related to the geostrophic wind speed  $G$  through the geostrophic balance. The effect of the bottom wall on the flow is modelled with classic Monin–Obukhov similarity theory for neutral boundary

layers (Moeng, 1984; Allaerts and Meyers, 2017). This wall-stress boundary condition is only dependent on the surface roughness  $z_0$ , which we assume to be constant. The upper boundary conditions together with the standard and wave-free fringe-region techniques are described in the next sections.

## 2.2 Upper Boundary Condition

Two different types of non-reflective upper boundary conditions are investigated in the current study, that is the RDL and the RC.

The RDL was initially introduced by Klemp and Lilly (1977) to damp out mountain-induced gravity waves at the top of the domain. It consists of an additional term on the right-hand side of the momentum equations which forces the flow to an unperturbed state, therefore dissipating the upward energy transport. This body force is applied within a sponge layer located at the top of the domain and reads as

$$f_i^{ra}(\mathbf{x}) = -\nu(z) \left( u_i(\mathbf{x}) - U_{G,i} \right)$$

where  $U_{G,1} = G \cos \alpha$ ,  $U_{G,2} = G \sin \alpha$  and  $U_{G,3} = 0$  with  $\alpha$  the geostrophic wind angle. The buffer layer performance depends on the Rayleigh function  $\nu(z)$ . This one-dimensional function should increase gradually with height to minimize wave reflection and it should be strong enough to dissipate upward-going energy. To this end, we choose

$$\nu(z) = \tilde{\nu} \left[ 1 - \cos \left( \frac{\pi}{s^{ra}} \frac{z - (L_z - L_z^{ra})}{L_z^{ra}} \right) \right]$$

where  $\tilde{\nu}$  is an inverse decay time and controls the force magnitude while  $s^{ra}$  regulates the function gradient along the vertical direction. Moreover,  $L_z$  and  $L_z^{ra}$  denote the height of the computational domain and of the RDL, respectively. Klemp and Lilly (1977) and Allaerts and Meyers (2017, 2018) chose a similar Rayleigh function with  $s^{ra} = 1$ . Instead, we consider this as a free parameter. Moreover, we scale  $\tilde{\nu}$  with the Brunt–Väisälä frequency, i.e.  $\tilde{\nu} = \nu^{ra} N$  with  $N = \sqrt{g\Gamma/\theta_0}$ , where  $\Gamma$  denotes the lapse rate in the free atmosphere. Hence, the RDL performance depends upon the choice of the non-dimensional parameters  $\nu^{ra}$  and  $s^{ra}$  while its computational efficiency is related to the number of vertical grid points spread over  $L_z^{ra}$ . The tuning of these parameters is performed in Sect. 3.1. Figure 1a shows the Rayleigh function obtained with  $L_z^{ra} = 10$  km,  $\nu^{ra} = 3$  and different  $s^{ra}$  values. We verified that if  $\nu(z)$  is properly calibrated, the boundary condition specified at the top of the domain has limited influence on the numerical solution. Here, we impose zero shear and zero vertical velocity.

Next, we have implemented the RC proposed by Klemp and Durran (1982) and Bougeault (1982). They were the first ones to propose an exact RC for the linear hydrostatic Boussinesq equations with a homogenous mean state in the absence of the Coriolis force, which reads as

$$\frac{1}{\rho_0} \hat{p}(k, l, z_T, t) = \frac{N}{(k^2 + l^2)^{1/2}} \hat{w}(k, l, z_T, t) \quad (4)$$

where  $\hat{p}$  and  $\hat{w}$  represent the horizontal Fourier coefficients of the pressure and vertical velocity, respectively, taken at the top of the domain  $z_T$ . Note that  $z_T = L_z - L_z^{ra}$  when the RC is used. Moreover,  $k$  and  $l$  denote the wavenumber in the  $x$ - and  $y$ -direction. Equation 4 shows that pressure and vertical velocity are related by a positive and time-independent quantity. The implication is twofold. First, a positive correlation between pressure and vertical velocity ensures a positive energy flux at the top of the domain. Second, the condition is local in time, avoiding the need of Laplace transforms. Despite the fact that the RC in Eq. 4 has been derived for linear hydrostatic Boussinesq equations, Klemp and Durran (1982) show that this upper boundary condition performs well even when these assumptions are violated. However, in such a case, Eq. 4 is not exact anymore, therefore partial wave reflection may be expected. The use of a RC



implies  $f_i^{ra} = 0$  and a computational domain height of  $L_z - L_z^{ra}$  instead of  $L_z$  in case of Rayleigh damping.

Internal gravity waves have an intrinsic property so that the sign of the vertical phase velocity is opposite to the sign of the vertical group velocity. The method developed by Taylor and Sarkar (2007) and later adopted by Allaerts and Meyers (2017, 2018) makes use of this property to distinguish upward from downward going waves in a frequency domain. Next, an inverse Fourier transform yields the vertical velocity perturbations divided into upward and downward internal waves. Similarly to Allaerts (2016); Allaerts and Meyers (2017), the corresponding vertical kinetic energy is then computed over a  $x$ - $z$  plane including the free atmosphere only without the buffer regions. The ratio between the vertical kinetic energy associated with downward and upward internal waves is what we define as reflectivity  $r$ . Since the only momentum sink which triggers gravity waves is located at the surface, internal waves transporting energy downward are solely due to reflection from the top of the domain. Therefore, the closer  $r$  is to zero, the better the upper boundary condition performs.

### 2.3 Fringe-Region Technique

A volume force applied within the fringe region is used to impose the desired inflow conditions, which we denote with  $u_{\text{in},i}(\mathbf{x})$ . The fringe forcing term reads as

$$f_i^{fr}(\mathbf{x}) = -h(x) \left( u_i(\mathbf{x}) - u_{\text{in},i}(\mathbf{x}) \right)$$

where  $h = h(x)$  is a one-dimensional non-negative function which is non-zero only within the fringe region, and is expressed as

$$h(x) = h_{\text{max}} \left[ F \left( \frac{x - x_s^h}{\delta_s^h} \right) - F \left( \frac{x - x_e^h}{\delta_e^h} + 1 \right) \right]$$

with

$$F(x) = \begin{cases} 0, & \text{if } x \leq 0 \\ \frac{1}{1 + \exp \left( \frac{1}{x-1} + \frac{1}{x} \right)}, & \text{if } 0 < x < 1 \\ 1, & \text{if } x \geq 1. \end{cases}$$

We choose this expression for the function  $F(x)$  since it has the advantage of having continuous derivatives of all orders (Lundbladh et al., 1999; Nordstrom et al., 1999). The parameters  $x_s^h$  and  $x_e^h$  denote the start and end of the fringe function support while its smoothness is regulated by  $\delta_s^h$  and  $\delta_e^h$ . Moreover,  $h_{\text{max}}$  denotes the maximum value of the fringe function. This technique, which we refer to as the standard fringe-region method, causes negligible disturbances in the surrounding flow when applied to pressure-driven boundary layer flows (Nordstrom et al., 1999; Goit and Meyers, 2015; Munters et al., 2016a). However, when applied to CNBL or stable boundary layer (SBL) flows, this body force displaces vertically air parcels with different temperatures while restoring the inflow condition. As a result, spurious gravity waves are triggered which propagate through the domain of interest, causing a distortion of the vertical velocity field which in turns perturbs the streamwise velocity and pressure fields.

To overcome this issue, we propose a new technique which imposes the desired inflow while locally damping the convective term in the vertical momentum equation. To this end, we define the following damping function

$$d(x, z) = 1 - \left[ F \left( \frac{x - x_s^d}{\delta_s^d} \right) - F \left( \frac{x - x_e^d}{\delta_e^d} + 1 \right) \right] \mathcal{H}(z - H) \quad (5)$$

where  $x_s^d$  and  $x_e^d$  define the start and end of the damping function support while  $\delta_s^d$  and  $\delta_e^d$  control the function smoothness. Moreover,  $H$  denotes the capping-inversion base height (which

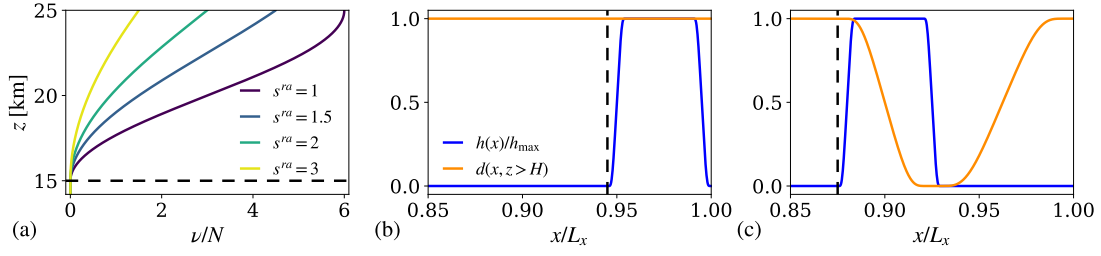


**Fig. 1** (a) Rayleigh function obtained with  $\nu^{ra} = 3$  and different  $s^{ra}$  values. (b) Fringe and damping functions used with the standard fringe-region technique. The fringe function parameters are set to  $x_s^h = 0.945L_x$ ,  $x_e^h = L_x$  and  $\delta_s^h = \delta_e^h = 0.01L_x$  while  $d(x, z) = 1$  everywhere. (c) Fringe and damping functions used with the wave-free fringe-region technique. The fringe function parameters are set to  $x_s^h = 0.875L_x$ ,  $x_e^h = 0.93L_x$  and  $\delta_s^h = \delta_e^h = 0.01L_x$  while the damping function ones are fixed to  $x_s^d = x_s^h$ ,  $x_e^d = L_x$ ,  $\delta_s^d = 0.05L_x$  and  $\delta_e^d = 0.075L_x$ . Note that  $L_x$  denotes the streamwise domain length. Moreover,  $h_{\max} = 0.03 \text{ s}^{-1}$  as in Allaerts and Meyers (2017, 2018). Finally, the black horizontal and vertical dashed lines denote the start of the RDL and the fringe region

also corresponds to the ABL height) while  $\mathcal{H}$  represents a Heaviside function. We note that a height-dependent damping function is necessary in case of a turbulent inflow profile. In fact, if the damping would be applied also within the ABL, not only spurious gravity waves would be dampened but also turbulence fluctuations (see Sect. 5 for more details). The modified vertical momentum equation then corresponds to

$$\frac{\partial u_3}{\partial t} + d(x_1, x_3) \frac{\partial}{\partial x_j} (u_j u_3) = g \frac{\theta - \theta_0}{\theta_0} - \frac{\partial \tau_{3j}^{sgs}}{\partial x_j} - \frac{1}{\rho_0} \frac{\partial p^*}{\partial x_3} - \frac{1}{\rho_0} \frac{\partial p_\infty}{\partial x_3} + f_3^{tot}.$$

Note that in boundary-layer flows the terms  $\partial(u_2 u_3)/\partial x_2$  and  $\partial(u_3 u_3)/\partial x_3$  have a smaller order of magnitude than the term  $\partial(u_1 u_3)/\partial x_1$ . Therefore, for the cases that we have examined in this work, we found that similar results are obtained if the local damping would be applied only to  $\partial(u_1 u_3)/\partial x_1$  (results not further discussed here).

We did extensive testing on the fringe and damping-function setups (results not shown in detail), and found that the technique is effective when the damping function is zero in the region where the fringe function decreases from  $h_{\max}$  to zero. Moreover, we notice that the new fringe-region technique performs well when enough grid points along the streamwise direction (at least 8 according to our tests) are located in the region where  $d(x, z) = 0$ , which is usually the case given the fine horizontal grid resolution of LES performed nowadays (Allaerts and Meyers, 2017, 2018; Gadde and Stevens, 2021; Lanzilao and Meyers, 2022). Furthermore, a smooth damping function in the  $x$ -direction is needed to avoid numerical oscillations. Finally, we note that the fringe forcing should be strong enough to force the desired inflow condition without violating the stability constraint imposed by the 4th order Runge-Kutta method, i.e.  $h_{\max} \Delta t \leq 2.78$  with  $\Delta t$  denoting the time step (Schlatter et al., 2005). If these constraints are satisfied, the inflow profile is correctly imposed and the fringe-induced gravity waves remain trapped within the fringe region, avoiding the distortion of the velocity and pressure fields downstream. Figure 1b, c shows the setup of the standard and wave-free fringe and damping functions, respectively, obtained following the guidelines defined above. The support, shape and maximum of the fringe function are equal in both cases. However, a longer buffer region is necessary with the new technique to allow room for a sufficiently smooth damping function. With the current setup, 12.5% of the total grid cells in the main domain are located within the fringe region when the new technique is employed while this number reduces to 5.5% for the standard method. The length of the fringe region, which we denote with  $L_x^{fr}$ , is determined as  $x_e^h - x_s^h$  and  $\max\{x_e^h, x_e^d\} - \min\{x_s^h, x_s^d\}$  in the standard and wave-free fringe-region technique, respectively.

### 3 Two-Dimensional Inviscid-Flow Simulations

In a first step, we test the fringe-region techniques together with the non-reflective upper boundary conditions in a two-dimensional ( $x$ - $z$ ) inviscid-flow environment. Here, the use of the sub-grid scale model is not necessary. The absence of viscous forces allows us to perform simulations with a relatively coarse grid resolution. Moreover, the flow is not driven by a background pressure gradient. Instead, a unidirectional and constant with height inflow velocity profile (i.e.  $u_{\text{in},1}(\mathbf{x}) = U_\infty$  and  $u_{\text{in},2}(\mathbf{x}) = u_{\text{in},3}(\mathbf{x}) = 0$  with  $\alpha = 0^\circ$ ), which is imposed within the fringe region, drives the flow. To comply with the assumptions on the inflow velocity profile, the Coriolis force and the wall stress are not applied. Instead, a symmetry boundary condition is used at the bottom. The potential temperature profile consists of a neutral ABL capped by an inversion layer with height  $H$ , strength  $\Delta\theta$  and depth  $\Delta H$  and a free atmosphere aloft with a constant lapse rate  $\Gamma$ . We use the model developed by Rampanelli and Zardi (2004) to define such a temperature profile, which characterizes a CNBL. Finally, a smooth box-like force model with length scale  $L_x^s$  emulates the presence of a wind-farm, generating a momentum sink within the ABL (see Appendix 1 for more details). These choices make the flow solver several orders of magnitude faster than standard LES of wind farms, allowing us to easily explore the parameter spaces of interest. Note that this setup is inspired by the work of Allaerts (2016), Appendix C.

Next, we non-dimensionalize the governing equations using a recurring set of three variables, that is the inflow velocity  $U_\infty$ , the height of the capping inversion  $H$  and the surface temperature  $\theta_0$ . This allows us to derive the following non-dimensional groups

$$\pi_g = \frac{gH}{U_\infty^2}, \quad \pi_{\Delta H} = \frac{\Delta H}{H}, \quad \pi_{\Delta\theta} = \frac{\Delta\theta}{\theta_0}, \quad \pi_\Gamma = \frac{\Gamma H}{\theta_0}, \quad \pi_L = \frac{L_x^s}{H}. \quad (6)$$

In the remainder of this section, we fix  $U_\infty = 12 \text{ m s}^{-1}$ ,  $H = 1000 \text{ m}$ ,  $\Delta H = 100 \text{ m}$  and  $\theta_0 = 288.15 \text{ K}$ , which define  $\pi_g = 68.125$  and  $\pi_{\Delta H} = 0.1$ . Next, we will first select a set of  $\pi_{\Delta\theta}$ ,  $\pi_\Gamma$  and  $\pi_L$  values for tuning the RDL in Sect. 3.1. We will use these cases to analyze in detail the flow response to the momentum sink applied within the ABL when four different numerical setups are used in Sect. 3.2. Finally, we perform a sensitivity analysis of several quantities of interest by extensively varying  $\pi_{\Delta\theta}$ ,  $\pi_\Gamma$  and  $\pi_L$  in Sect. 3.3. We note that the Froude ( $Fr$ ) and  $P_N$  numbers can be written as  $Fr = 1/\sqrt{\pi_g \pi_{\Delta\theta}}$  and  $P_N = 1/\sqrt{\pi_g \pi_\Gamma}$ , meaning that we will effectively vary the two non-dimensional quantities that characterize the impact of gravity waves on the flow dynamics (Smith, 2010; Allaerts and Meyers, 2018, 2019; Lanzilao and Meyers, 2021).

#### 3.1 Tuning of the RDL Parameters

In this section, we tune the RDL by performing approximately thousand simulations sweeping through the  $\nu^{ra}-s^{ra}$  parameter space in search of the values that minimize the reflectivity. To do so, we use the atmospheric states and box-like forcing region lengths considered by Allaerts (2016). Hence, we set  $\pi_{\Delta H} = 0.1$  and  $\pi_{\Delta\theta} = 3.47 \times 10^{-3}$  which correspond to a capping inversion 100 m deep with a strength of 1 K. For the free atmosphere, we use two values of  $\pi_\Gamma$ , that is  $3.47 \times 10^{-3}$  and  $3.47 \times 10^{-2}$ , which corresponds to a weakly and strongly stratified atmosphere. Further, we fix two values of  $\pi_L$ , i.e. 5 and 15. Note that the force integrated over the whole computational domain has equal magnitude for the two cases (see Appendix 1), which therefore emulate the presence of a small dense ( $\pi_L = 5$ ) and a large sparse ( $\pi_L = 15$ ) wind farm. For the computational domain, we fix the length and height to 40 km and 25 km, which is in accordance with previous studies (Allaerts and Meyers, 2017, 2018). In the horizontal direction we use a uniform grid with  $N_x = 256$  grid points, while in the vertical direction a stretched grid is used. The latter is composed of 300 uniformly spaced grid points within the first 1.5 km. A first stretch is applied from 1.5 km to 15 km, where 180 points are used. A second one is applied within the RDL, i.e from 15 km to 25 km (i.e.  $L_z^{ra} = 10 \text{ km}$ ). We have tested several grid stretchings within the RDL spanning from 100 to 5 grid points and we have noticed that 10 grid points suffice to damp out waves before they reach the top of the domain (not shown). However, we

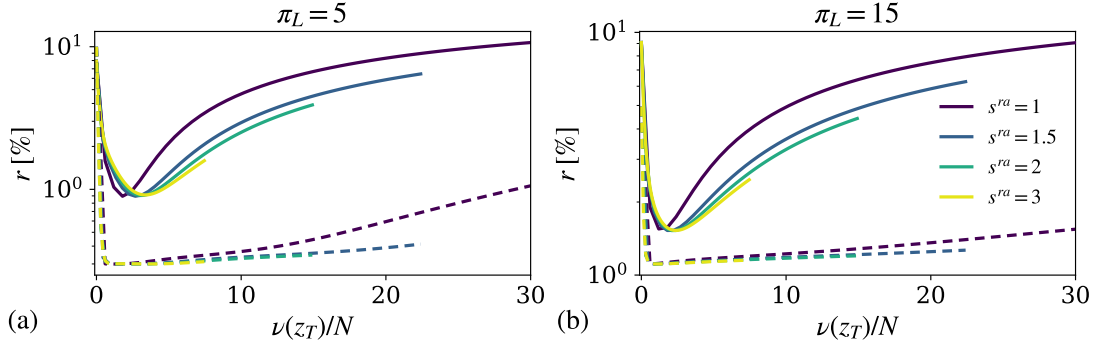


**Fig. 2** Reflectivity as function of  $\nu(z_T)/N$  (i.e. the maximum Rayleigh function value normalized with the Brunt–Väisälä frequency) obtained with (a)  $\pi_L = 5$  and (b)  $\pi_L = 15$ . The parameter  $\nu^{ra}$  is varied between 0 and 15 while  $s^{ra}$  varies between 1 and 3. The solid and dashed lines refer to results obtained with  $\pi_\Gamma = 3.47 \times 10^{-3}$  (weakly stratified atmosphere) and  $\pi_\Gamma = 3.47 \times 10^{-2}$  (strongly stratified atmosphere), respectively. Note that the  $y$ -axis is in logarithmic scale

note that we did not perform sensitivity tests on the height of the RDL. Instead, we used the same  $L_z^{ra}$  adopted in previous studies (Allaerts and Meyers, 2017, 2018). These choices make the RDL extremely efficient, since only the 2% of vertical grid points are located in this region. To summarize, the vertical grid contains a total of 490 grid points.

The reflectivity as function of  $\nu(z_T)/N$  (i.e. the maximum Rayleigh function value normalized with the Brunt–Väisälä frequency - see Fig. 1a) is shown in Fig. 2. Here, we vary  $\nu^{ra}$  between 0 and 15 and  $s^{ra}$  between 1 and 3. Setting  $\nu^{ra}$  to zero corresponds to a case without RDL, for which the reflectivity is about 10% in all cases. As  $\nu^{ra}$  increases, the reflectivity reaches a global minimum, increasing monotonically afterwards. Such a minimum is almost insensitive to the choice of  $s^{ra}$ . Similar trends have been observed by Klemp and Lilly (1977). For both  $\pi_L$  values, the reflectivity is low and rather constant to changes in the Rayleigh function when  $\pi_\Gamma = 3.47 \times 10^{-2}$  (strongly stratified atmosphere). This is explained by the fact that  $L_z^{ra}$  is approximately  $5/2$  times the gravity-wave vertical wavelength  $\lambda_z$ , which is evaluated as  $2\pi U_\infty/N$ . Conversely, a higher sensitivity is observed when  $\pi_\Gamma = 3.47 \times 10^{-3}$  (weakly stratified atmosphere), where the  $L_z^{ra}$  to  $\lambda_z$  ratio is roughly one. Figure 2 also shows that a non-tuned RDL could lead to a higher reflectivity than a setup without RDL, highlighting the importance of properly calibrating the Rayleigh function. The minimum reflectivity value in all atmospheric states is attained with the parameters  $\nu^{ra} = 3$  and  $s^{ra} = 2$ , which we use to tune the RDL. The Rayleigh function obtained with these parameters is shown in Fig. 1a. In contrast to the RDL, the RC is parameter-free, therefore there is no need to perform a calibration study. Moreover, the vertical grid contains 480 points instead of 490 when the RC is adopted.

### 3.2 Flow Physics

To show the differences in the numerical solution between a standard upper boundary condition and a non-reflective one, we use the standard fringe-region technique without and with the tuned RDL and we name these cases as stdFR-woRDL and stdFR-RDL, respectively. Next, we adopt the new fringe-region technique together with the tuned RDL (newFR-RDL). The comparison between cases stdFR-RDL and newFR-RDL will highlight the benefits of using a wave-free fringe-region technique. Finally, we use the new fringe-region method together with the RC (newFR-RC). The newFR-RDL and newFR-RC cases allow us to assess the performances of the two different non-reflective upper boundary conditions. Since adopting the standard fringe-region technique with the RC would not bring further insights, we decided to not consider this case. Hence, we have a total of four different numerical setups which we drive with the same atmospheric states and box-like force term that were used in Sect. 3.1.

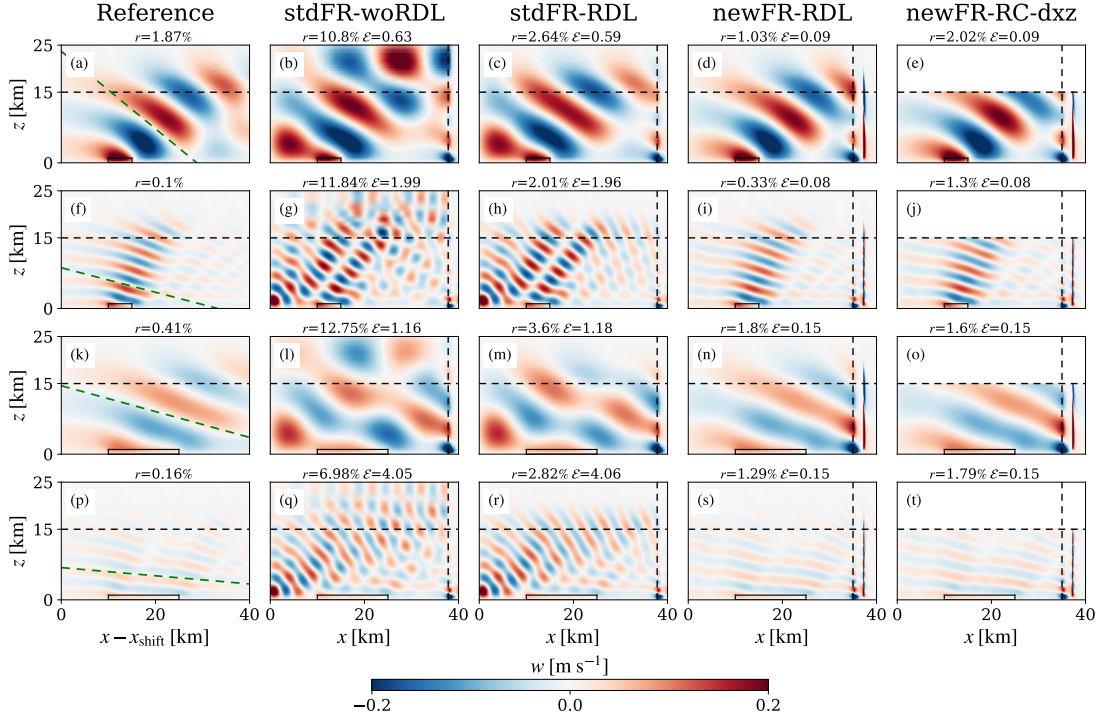


**Fig. 3** Side view of vertical velocity obtained with (a-e)  $\pi_L = 5$  and  $\pi_\Gamma = 3.47 \times 10^{-3}$ , (f-j)  $\pi_L = 5$  and  $\pi_\Gamma = 3.47 \times 10^{-2}$ , (k-o)  $\pi_L = 15$  and  $\pi_\Gamma = 3.47 \times 10^{-3}$  and (p-t)  $\pi_L = 15$  and  $\pi_\Gamma = 3.47 \times 10^{-2}$ . Note that the solution in the reference domain is shifted of  $x_{\text{shift}} = 90$  km. The black solid lines denote the region in which the box-like force term is applied. The black horizontal and vertical dashed lines indicate the starting location of the RDL and the fringe region. Finally, the green dash-dotted line in (a,f,k,p) denotes the inclination of the gravity-wave phase line predicted by linear theory

The simulations are performed on a domain with length  $L_x = 40$  km, as in Sect. 3.1. However, we vary  $N_x$  from 256 to 1000, leading to a horizontal grid resolution of 40 m. The grid sensitivity study performed in Appendix 2 shows that this change has almost no impact on the reflectivity value, and that the numerical solution is grid independent. Finally, we define two simulations which are performed on a domain five times longer (i.e. 200 km long) with an equal grid resolution. Both simulations adopt the tuned RDL, but one makes use of the standard fringe region-technique (stdFR-RDL-LD) while the second employs the new technique (newFR-RDL-LD). We show in Appendix 3 that the length of the domain is large enough for the newFR-RDL-LD solution to be not affected by the boundary conditions. Consequently, the numerical solutions obtained on the small domain of 40 km will be compared against the newFR-RDL-LD solution in the remainder of this section. For this reason, the latter case will be also named as the reference (Reference). In all cases, the time horizon is set to  $T = 2$  h. At this point, a stationary gravity-wave pattern has formed and the flow has reached a steady state (Allaerts, 2016).

Gravity waves are triggered by the box-like force term applied within the ABL and propagate through the free atmosphere. Figure 3a, f, p shows the vertical velocity contours obtained with the reference setup together with a dash-dotted green line which represents the angle that the gravity-wave phase lines make with the horizontal. This angle is calculated using linear theory as  $\arccos(k_x U_\infty / N)$  with  $k_x = 1/L_x^s$  (Lin, 2007). Good agreement between reference simulations and linear theory is found for all  $\pi_\Gamma$  and  $\pi_L$  values. Moreover, the highest vertical velocity value is found near the leading edge of the box-like forcing region, as a response to the momentum sink applied within the ABL. Next, Fig. 3b, g, l, q displays the results obtained with the stdFR-worDL setup. Here, it is evident how the fringe body force also triggers spurious gravity waves which heavily perturb the flow field downstream, altering the gravity-wave phase lines. This is

particularly noticeable when a strong free lapse rate is used. The same phenomenon is observed in the stdFR-RDL case, where the maximum  $w$  value is attained near the inflow region instead of at the leading edge of the box-like forcing region. Conversely, the new fringe-region technique traps the spurious gravity waves within the fringe region by damping the convective term in the vertical momentum equation. This is visible in the newFR-RDL and newFR-RC cases. As a result, the numerical solution within and around the box-like forcing region is very similar to the reference one, despite using a domain which is five times smaller in length.

In terms of reflectivity, high values are obtained when a RDL is not used. However, results show that the reflectivity can be reduced by one order of magnitude when the RDL is tuned properly. For instance, the reflectivity obtained in Fig. 3g, h decreases from 11.84% to 2.01%. This highlights the importance of properly tuning the Rayleigh function in such simulations, as previously pointed by Allaerts (2016). Conversely, the difference between the tuned RDL and the RC is more marginal, with the RDL outperforming the RC in three out of the four cases, reaching a minimum reflectivity value of 0.33%. Overall, simulations with  $\pi_\Gamma = 3.47 \times 10^{-3}$  show higher reflectivity when compared to simulations with  $\pi_\Gamma = 3.47 \times 10^{-2}$ , which is again relatable to the  $L_z^{ra}/\lambda_z$  ratio.

Next, we define the following error quantity

$$\mathcal{E} = \frac{\max_{x \in [0, L_x - L_x^{fr}]} \{|w^{\text{Ref}}(x + x_{\text{shift}}, z) - w(x, z)|\}}{\max_{x \in [0, L_x^{\text{Ref}} - L_x^{fr}]} \{w^{\text{Ref}}(x, z)\}}$$

where  $w^{\text{Ref}}(x, z)$  denotes the vertical velocity field obtained with the reference setup. Moreover,  $x_{\text{shift}} = 90$  km so that we compare both solutions around the box-like forcing region. The idea behind this metric is to quantify the amplitude of the spurious gravity waves triggered by the fringe body force in the domain of interest with respect to the amplitude of the gravity waves triggered by the box-like force term in the reference simulation. Figure 3 shows that  $\mathcal{E}$  is almost insensitive to the upper boundary condition. However, the new fringe-region technique reduces  $\mathcal{E}$  considerably. For instance,  $\mathcal{E} \approx 4$  in Fig. 3q, r, meaning that the amplitude of the fringe-induced gravity waves is four times the maximum gravity-wave amplitude triggered by the box-like force term in the reference solution. Conversely,  $\mathcal{E} = 0.15$  when the wave-free fringe-region technique is applied, that is in Fig. 3s, t.

The gravity waves shown in Fig. 3 are triggered by the inversion layer displacement, which we denote with  $\eta$ . This quantity is shown in Fig. 4a-d for all simulation setups. Note that  $\eta$  represents a streamline which is computed starting from  $x = 0$  and  $z = H$ . The reference simulation results show that a strongly stratified free atmosphere limits the vertical displacement of air parcels, therefore contributing to a lower capping inversion displacement. Very good agreement with the reference solutions is found when the wave-free fringe-region technique is applied. Conversely, the use of the standard fringe-region technique causes an overestimation of  $\eta$  together with an oscillation near the inflow region. The latter is particularly visible when  $\pi_\Gamma = 3.47 \times 10^{-2}$ .

Next, the gravity-wave induced pressure perturbations along the  $x$ -direction taken at  $z = H$  are shown in Fig. 4e-h. Typical unfavourable and favourable pressure gradients are observed in front of and through the box-like forcing region, respectively (Smith, 2010; Allaerts and Meyers, 2017, 2018, 2019). However, the standard fringe-region technique overestimates the pressure build-up in the zone in front of the box-like forcing region when compared against the reference solution. This is expected, since a higher capping inversion displacement amplifies the cold temperature anomaly resulting in higher pressure perturbations within the ABL (Smith, 2010; Allaerts and Meyers, 2017). Conversely, the solution obtained with the wave-free fringe-region method match well with the reference one in all cases.

Pressure perturbations can also be evaluated using linear theory. Given the Fourier coefficients of the reference simulation capping inversion displacement  $\hat{\eta}^{\text{Ref}}(k)$ , the pressure Fourier coefficients given by linear theory, denoted with  $\hat{p}^{\text{LT}}(k)$ , are computed as

$$\frac{1}{\rho_0} \hat{p}^{\text{LT}}(k) = \left( \frac{g \Delta \theta}{\theta_0} + i \frac{N^2 - k^2 U_\infty^2}{\sqrt{N^2/U_\infty^2 - k^2}} \right) \hat{\eta}^{\text{Ref}}(k)$$

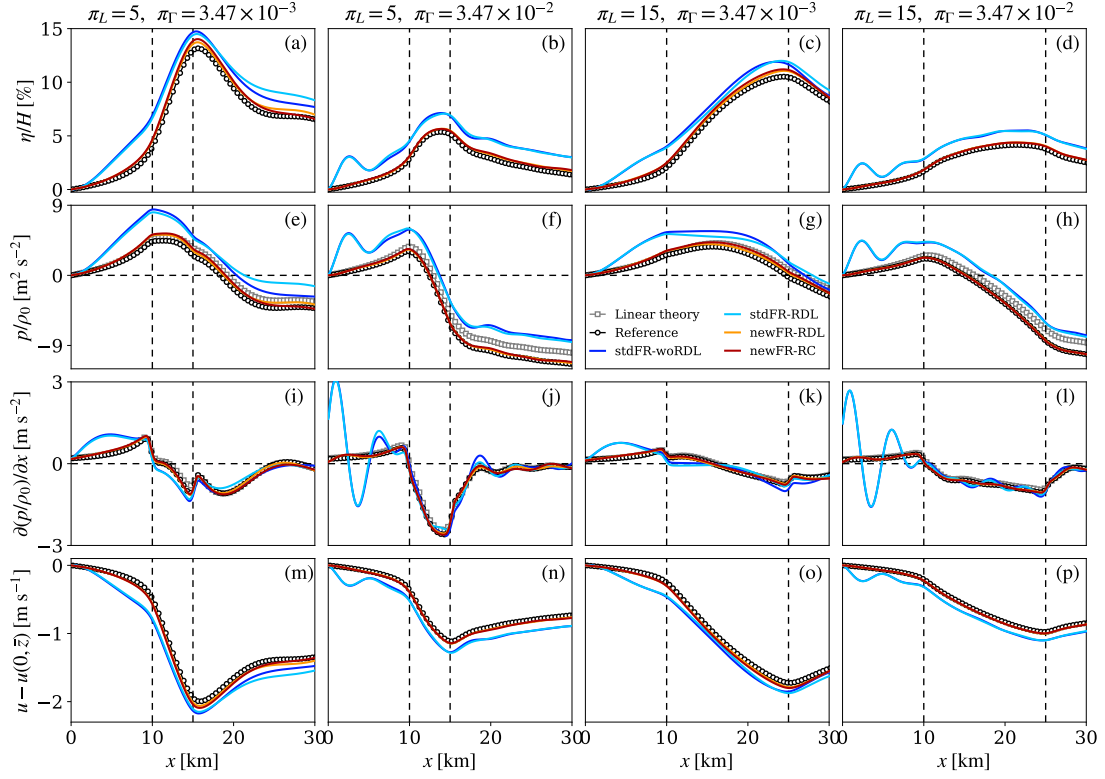


**Fig. 4** (a-d) Capping inversion displacement, (e-h) pressure perturbation at  $z = H$ , (i-l) streamwise pressure gradient at  $z = H$  and (m-p) velocity perturbation at  $\bar{z} = 100$  m evaluated with linear theory and with the different numerical setups. The vertical dashed lines denote the box-like forcing region

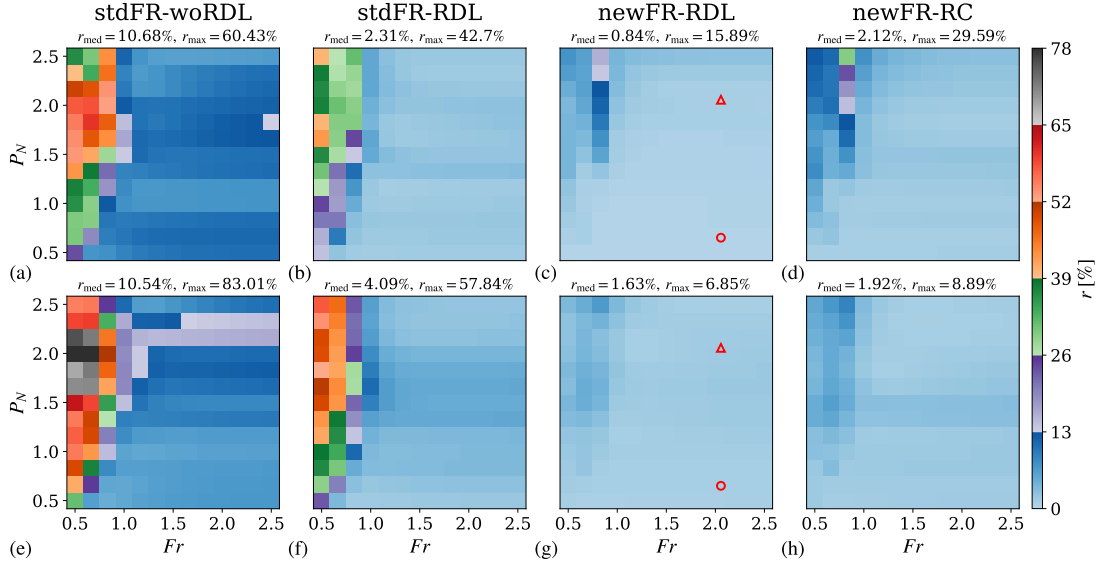
where  $i = \sqrt{-1}$  (Gill, 1982; Nappo, 2002; Lin, 2007; Smith, 2010; Allaerts and Meyers, 2019). Figure 4e-h illustrates that the newFR-RDL, newFR-RC and reference pressure profiles agree well with results from linear theory in all cases. However, an offset which increases along the streamwise direction is observed. We hypothesize that this offset is caused by non-linear effects. In fact, the reference, newFR-RDL and newFR-RC profiles coincide with linear theory at  $z = 10$  km, where the perturbations amplitude has decreased considerably (not shown). The more accurate pressure profiles obtained with the wave-free fringe-region technique translate in more accurate pressure gradient predictions particularly in front of the box-like forcing region, as shown in Fig. 4i-l.

Finally, Fig. 4m-p shows the velocity perturbation at  $\bar{z} = 100$  m. In all cases, the velocity profiles obtained with the standard fringe-region technique follow the reference solution trend within and downwind the forcing region. However, large discrepancies are observed upwind, where the profiles depart from the reference ones. Contrarily, an excellent match is observed when the wave-free fringe-region method is used.

### 3.3 Sensitivity Analysis

We now study how the reflectivity and  $\mathcal{E}$  vary with the atmospheric state and the length of the box-like force term. To this end, we use the same numerical setups adopted in Sect. 3.2. The only difference is that we make use of a coarser grid with  $N_x = 640$  to limit the computational cost. Moreover, we adopt the same  $\pi_g$ ,  $\pi_{\Delta H}$  and  $\pi_L$  values of Sect. 3.2 but we vary  $\pi_{\Delta\theta}$  and  $\pi_\Gamma$  so that the  $Fr$  and  $P_N$  values range from 0.5 to 2.5 for a total of 169 atmospheric states. This allows us to extensively explore the  $Fr$ - $P_N$  parameter space.





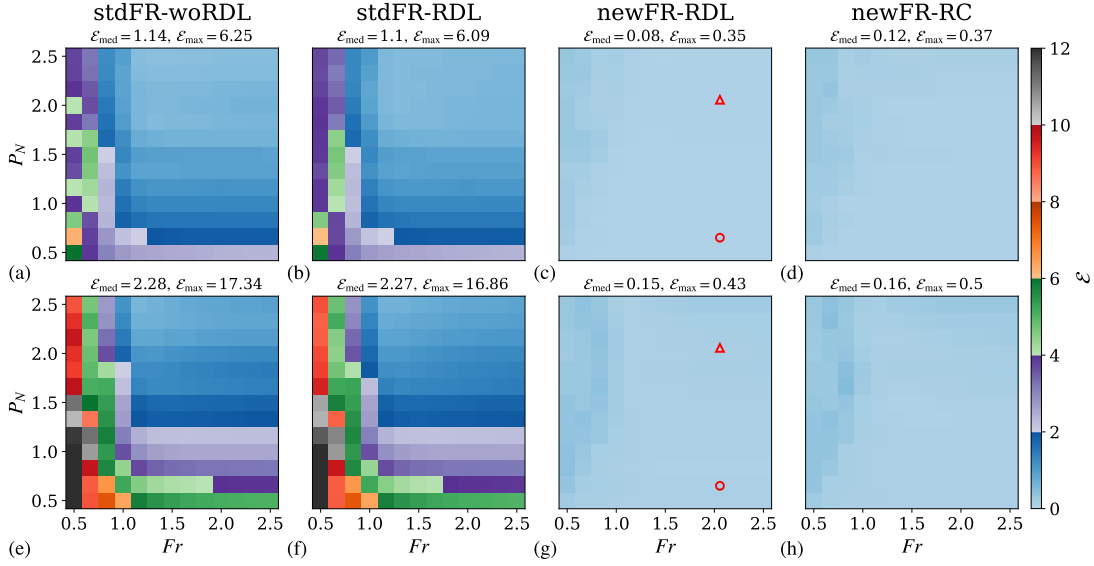
**Fig. 5** Reflectivity as function of the  $Fr$  and  $P_N$  numbers obtained with (a-d)  $\pi_L = 5$  and (e-h)  $\pi_L = 15$  using the different numerical setups. The symbols  $r_{\text{med}}$  and  $r_{\text{max}}$  denote the median and the maximum of the  $r$  distribution. The red triangle and circle mark the atmospheric states analyzed in details in Sect. 3.2

Figure 5a-d and Fig. 5e-h show the reflectivity obtained with the different numerical setups using  $\pi_L = 5$  and  $\pi_L = 15$ , respectively. The pattern observed for both  $\pi_L$  values are similar. In both cases, the reflectivity is rather constant along lines of low and constant  $P_N$  values while it shows a higher variability for higher  $P_N$ . This behaviour was also noted by Smith (2010) and Lanzilao and Meyers (2021), who observed that the flow response is less sensitive to changes in Froude number when  $P_N$  is low. The median of the reflectivity distribution obtained with  $\pi_L = 15$  in the stdFR-RDL and newFR-RDL cases differs of several percentage points, going from 4.1% to 1.6%. A more accentuate difference is observed in the maximum reflectivity value (see Fig. 5f, g). This illustrates that the absence of spurious gravity waves also reduces the amount of energy reflected downward. In terms of upper boundary conditions, the highest reflectivity values are obtained when a RDL or a RC are not used. For instance, reflectivity values above 80% are observed with the stdFR-woRDL setup. Finally, Fig. 5c, d and Fig. 5g, h show that the tuned RDL slightly outperforms the RC. The red triangle and circle in Fig. 5c, g denote the simulation setup and atmospheric state used to calibrate the Rayleigh function in Sect. 3.1.

A similar analysis has been conducted using  $\mathcal{E}$  as a metric. Results are shown in Fig. 6. We observe that the upper boundary condition has limited impact on such a metric. Contrarily, a clear difference is observed between the standard and wave-free fringe-region techniques, where the median of the  $\mathcal{E}$  distribution goes from 1.1 to 0.08 with  $\pi_L = 5$  and from 2.27 to 0.15 when  $\pi_L = 15$ . Higher values of  $\mathcal{E}$  are observed for subcritical flows and low  $P_N$  numbers when the standard fringe-region technique is used, with maximum values above 17 when  $\pi_L = 15$ . Conversely, the wave-free fringe-region technique shows low and rather constant values of  $\mathcal{E}$  across the whole  $Fr$ - $P_N$  parameter space.

The results of this sensitivity analysis point out that the wave-free fringe-region technique improves the quality of the numerical solution for all  $\pi_L$ ,  $\pi_{\Delta\theta}$  and  $\pi_\Gamma$  values considered. In terms of upper boundary conditions, the RC has the advantage to be parameter-free and it does not require an additional sponge layer. Conversely, the RDL needs to be tuned and requires a buffer layer. However, the computational overhead caused by the RDL in our setup is negligible due to the limited amount of vertical grid points used within the sponge layer. Moreover, the RDL outperforms the RC in all cases analyzed.





**Fig. 6**  $\varepsilon$  as function of the  $Fr$  and  $P_N$  numbers obtained with (a-d)  $\pi_L = 5$  and (e-h)  $\pi_L = 15$  using the different numerical setups. The symbols  $\varepsilon_{\text{med}}$  and  $\varepsilon_{\text{max}}$  denote the median and the maximum of the  $\varepsilon$  distribution. The red triangle and circle mark the atmospheric states analyzed in details in Sect. 3.2

#### 4 Three-Dimensional Inviscid-Flow Simulations

In this section we study the flow behaviour in an inviscid-flow environment with a three-dimensional computational domain. To this end, we fix the box-like forcing region length and width to  $L_x^s = 15$  km and  $L_y^s = 9$  km, respectively (see Appendix 1). This roughly corresponds to the area occupied by the London Array wind farm. The length and width of the computational domain are  $L_x = 100$  km and  $L_y = 80$  km with  $N_x = 1000$  and  $N_y = 800$ , which correspond to a squared grid with resolution of 100 m. The atmospheric states and tuning of the Rayleigh, fringe and damping functions correspond to the ones adopted in Sect. 3. Moreover, results obtained with the two-dimensional inviscid-flow simulations have shown that the tuned RDL provides accurate flow fields with lower values of reflectivity when compared against the RC. Therefore, in this section we only compare numerical results obtained with the stdFR-RDL and newFR-RDL setups.

Figure 7a-d illustrates top views of streamwise velocity fields taken at  $z = 100$  m. The velocity gradually decreases over the box-like forcing region, reaching a minimum value in proximity of the trailing edge. Moreover, the wake recovery is limited due to the absence of turbulent mixing. Similar results were obtained with a two-dimensional domain (see Fig. 4m-p). Note that the flow is symmetric with respect to the centreline of the domain, since the Coriolis force is neglected. Finally, at the end of the domain, the fringe-region technique forces the flow to  $U_\infty$ , breaking the periodicity. No major differences in terms of velocity perturbations are observed at a height of 100 m among the different numerical setups and  $\pi_L$  values. We remark though that this is not anymore the case in a LES environment (see Sect. 5). Next, Fig. 7e-h shows top views of streamwise velocity taken at  $z = 5$  km. The stronger free lapse rate decreases the gravity-wave vertical wavelength, therefore Fig. 7g, h shows velocity oscillations with a lower horizontal wavelength than the ones observed in Fig. 7e, f. As shown previously, the standard fringe-region technique triggers spurious gravity waves which perturb the vertical velocity field. Consequently, through the continuity constraint, the streamwise velocity field is also distorted. This is mainly visible when comparing Fig. 7g, h in the zone upwind of the box-like forcing region.

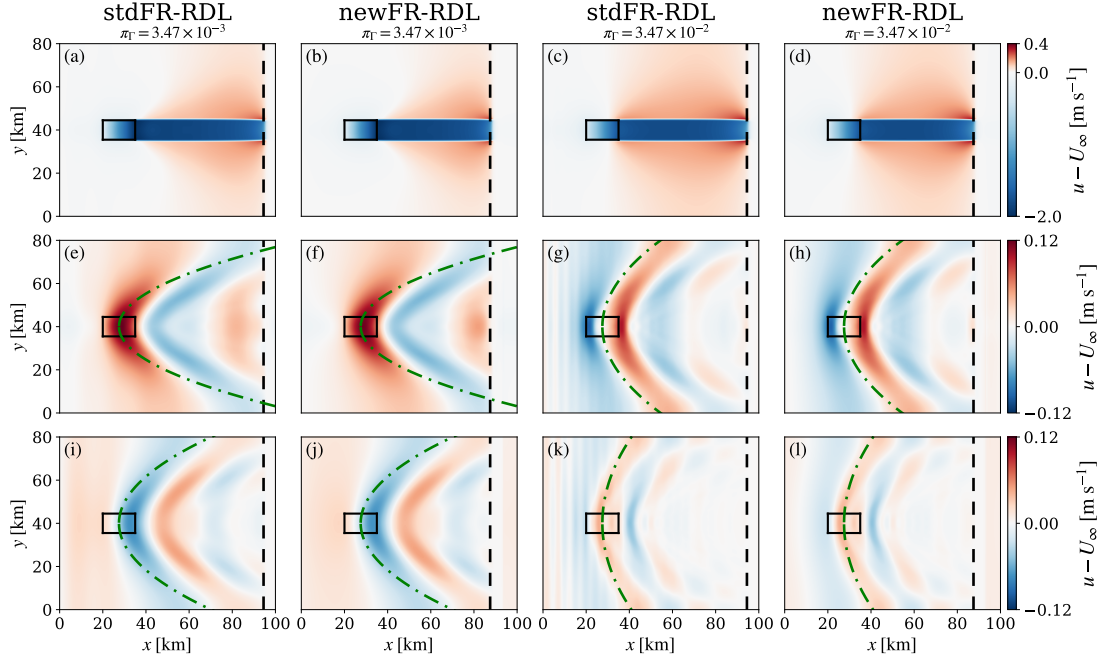


**Fig. 7** Top view of streamwise velocity taken at (a-d)  $z = 0.1$  km, (e-h)  $z = 5$  km and (i-l)  $z = 10$  km. The black solid lines denote the region in which the box-like force term is applied. The black dashed lines indicate the starting location of the fringe region. Finally, the green dash-dotted line denotes the parabola along which wave energy is trailed downstream by internal gravity waves

Smith (1980) derived analytically that the internal wave energy is transported downstream along parabolas given by

$$y^2 = \frac{Nax}{U_\infty} z, \quad a = (k_x^2 + l_y^2)^{-\frac{1}{2}}$$

when the flow is hydrostatic and the obstacle perturbing the flow consists of a bell-shape circular mountain. Note that  $a$  represents a characteristic length scale while  $k_x = 1/L_x^s$  and  $l_y = 1/L_y^s$  (Lin, 2007). The dash-dotted green line in Fig. 7e-l represents such parabola. Despite the fact that our solution is derived for a rectangular drag force, we still find a very good agreement with the theory of Smith (1980). Finally, Fig. 7g, h shows top views of streamwise velocity taken at  $z = 10$  km. The U-shaped gravity-wave pattern widen with height, and a good agreement between theory and simulation is still found. Even at this height, the oscillations triggered by the standard fringe-region technique are still visible, mainly in Fig. 7k.

## 5 Large-Eddy Simulations

In this section, the stdFR-RDL and newFR-RDL numerical setups are applied to an LES of a wind farm. The Coriolis force is now included in the momentum equations together with the wall stress and the sub-grid scale model, so that the full governing equations described in Sect. 2.1 are resolved. Moreover, a fully-developed turbulent inflow profile is used, which is provided by a concurrent precursor simulation. The case setup is described in Sect. 5.1 while results are shown in Sect. 5.2. In the remainder of the text, we use a bar to denote time-averaged quantities while spatial averages are denoted with angular brackets.

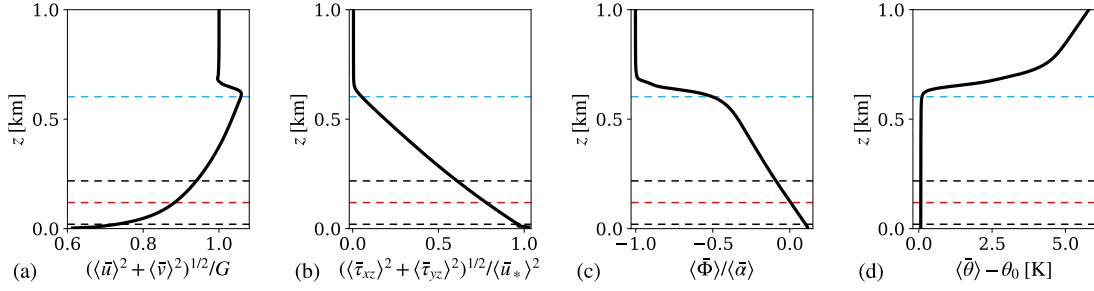


**Fig. 8** Vertical profiles, averaged over the full horizontal directions and over the last two hours of the precursor simulation, of (a) horizontal velocity magnitude, (b) total shear stress magnitude, (c) horizontal wind direction and (d) potential temperature. The red dashed line denotes the hub height while the black dashed lines are representative of the rotor dimension. Finally, the blue dashed line represents the boundary-layer height

### 5.1 Case Setup

We consider a large farm with 160 turbines disposed in 16 rows and 10 columns in a staggered pattern with respect to the main wind direction. The turbine-rotor diameter and hub height are  $D = 198$  m and  $z_h = 119$  m, which correspond to the dimensions of the IEA 10 MW offshore wind turbine (Bortolotti et al., 2019). Next, the streamwise and spanwise spacings are set to  $s_x D = s_y D = 5D$ , which lead to a farm length and width of 14.85 km and 9.4 km, respectively. The box-like force term is now replaced by wind turbines, which are modelled using a non-rotating actuator disk model with a disk-based thrust coefficient of  $C'_T = 4/3$ , which corresponds to a thrust coefficient of  $C_T = 0.75$  (Calaf et al., 2010; Goit and Meyers, 2015; Allaerts and Meyers, 2017; Lanzilao and Meyers, 2022). Moreover, a simple yaw controller is implemented to keep the turbine-rotor disk perpendicular to the incident wind flow.

The fringe and damping functions are tuned as reported in Sect. 2.3. To ensure a 10 km distance both upwind and downwind between the farm and the fringe region, we select a domain length of 40 km (Inoue et al., 2014; Allaerts and Meyers, 2017; Lanzilao and Meyers, 2022). Moreover, to minimize the sidewise blockage, we fix the width of the domain to 18 km. The grid resolution in the streamwise and spanwise directions is set to 31.25 m and 20 m, respectively. With such a resolution we have a total of 10 grid points along the turbine-rotor disk in the spanwise direction, which is similar to earlier studies (Calaf et al., 2010; Allaerts and Meyers, 2017). In the vertical direction, we adopt the same grid used in Sects. 3 and 4, that is a domain height of 25 km with 490 grid points, 10 of which lay within the RDL. The Rayleigh function is also tuned as in Sect. 3.1. In fact, at the height of 15 km, turbulence has decayed so that the velocity fields are constant with height and laminar, meaning that there is no need to re-tune the RDL. The precursor domain does not contain wind turbines nor a fringe region, therefore we select a streamwise length of 10 km. The lateral and vertical dimensions coincide with the ones of the main domain. The combination of precursor and main simulations leads to a total of  $705.6 \times 10^6$  grid cells, which is three orders of magnitude higher than the number of grid cells used in simulations performed in Sect. 3.

Similarly to previous sections, the atmospheric state is represented by a CNBL. The initial velocity profile in the mixed layer is provided by the Zilitinkevich (1989) model with parameters  $u_* = 0.375$  m s<sup>-1</sup> and  $z_0 = 2 \times 10^{-3}$  m, which represent the friction velocity and surface roughness, while the free atmosphere is characterized by a constant geostrophic wind  $G = 10.5$  m s<sup>-1</sup>. The two velocity profiles are then combined following the method proposed by Allaerts and Meyers (2015). Next, the Rampanelli and Zardi (2004) model is used to specify the vertical potential temperature profile. The ground temperature is fixed to  $\theta_0 = 282.5$  K. The base of the capping inversion is set to  $H_{in} = 580$  m while the capping inversion depth and strength are fixed to  $\Delta H = 175$  m and  $\Delta \theta = 3.8$  K, respectively. Finally, we select a free lapse rate of  $\Gamma = 5.1$  K km<sup>-1</sup>. We note that these initial velocity and potential temperature vertical profiles corresponds to the ones adopted in Lanzilao and Meyers (2022).

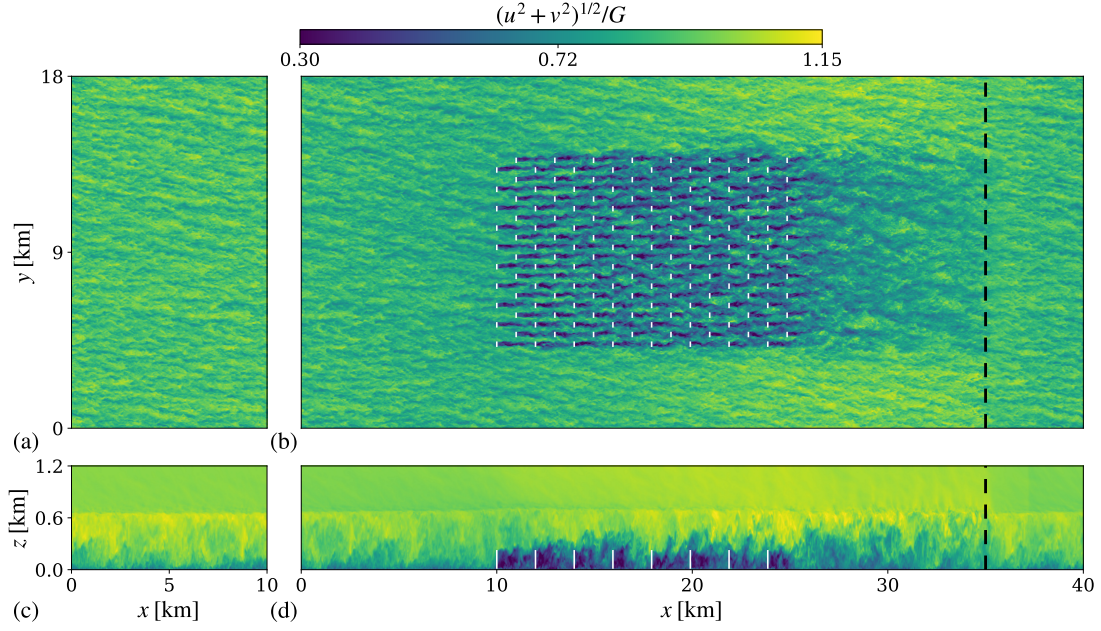


**Fig. 9** Instantaneous contours of horizontal velocity magnitude at  $T = 2$  h obtained with the newFR-RDL setup. Top view at hub height and side view at  $y = 8.258$  km (i.e. along the 5<sup>th</sup> turbine column) of (a,c) precursor and (b,d) main simulations. The wind-turbine rotors are denoted with white lines while the vertical black dashed lines indicate the starting location of the fringe region

We further add random divergence-free perturbations with amplitude of  $0.1G$  in the first 100 m to the vertical velocity profile. This initial state is given as input to the precursor simulation which is progressed in time for 20 h. At this point, a statistically steady state has been reached (Allaerts and Meyers, 2016, 2017). Figure 8 illustrates vertical profiles of several quantities averaged over the last two hours of simulation and over the horizontal directions. The boundary layer extends up to the capping inversion, located now at  $H = 630$  m, below which the total shear stress magnitude shows a close to linear profile. The direction of the flow at hub height is parallel to the  $x$ -direction (i.e.  $\langle \bar{\Phi} \rangle(z_h) = 0^\circ$ ). This is achieved by using the wind-angle controller developed by Allaerts and Meyers (2015). The velocity at hub height measures  $9.25 \text{ m s}^{-1}$  with a turbulence intensity of 5.35%. The friction velocity and the geostrophic wind angle are  $\langle \bar{u}_* \rangle = 0.361 \text{ m s}^{-1}$  and  $\langle \bar{\alpha} \rangle = -12.34^\circ$ . Finally, the  $Fr$  and  $P_N$  numbers are 1.18 and 1.12, respectively.

Next, we switch on the turbines in the main domain and we run main and precursor simulations in parallel. The turbulent fully-developed CNBL described above forms the inflow profile  $u_{in,i}(\mathbf{x})$ ,  $i = 1, 2, 3$  which is imposed by the standard and wave-free fringe-region techniques in the main domain. This second spin-up phase lasts for 1 h, which corresponds to approximately two wind-farm flow-through times. At this point, the boundary layer in the main domain has adapted to the additional drag force produced by the turbines and a statistically steady state has been reached again. This is suggested by the fact that negligible differences are observed in the numerical solution taken at subsequent time instances. Finally, the wind-angle controller in the precursor simulation is switched off and statistics are collected during a time window of 2 h.

## 5.2 Results

A typical flow response to wind-farm forcing is shown in Fig. 9, which displays instantaneous contours of velocity magnitude obtained at the end of the newFR-RDL simulation (i.e.  $T = 2$  h) for both the precursor and main domains. Figure 9a, c illustrates a top and side view of the

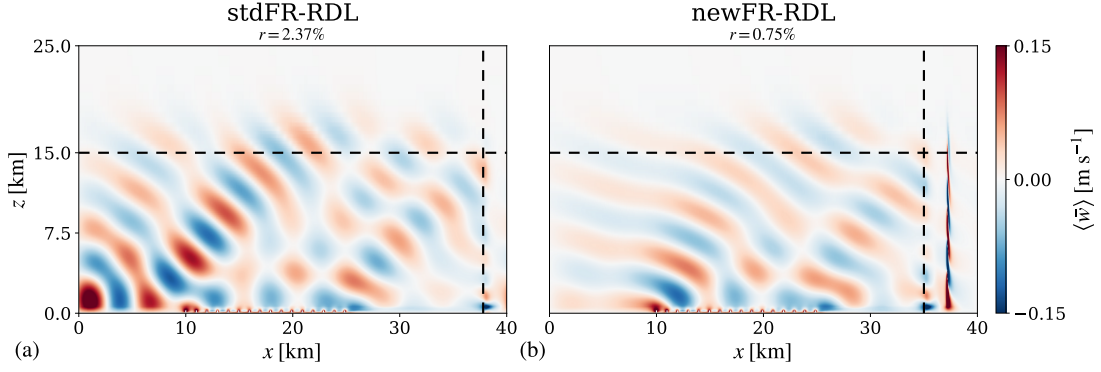


**Fig. 10** Contours of vertical velocity for cases (a) stdFR-RDL and (b) newFR-RDL, averaged over time and along  $x$ - $z$  planes within the turbine columns footprint (i.e. along all  $x$ - $z$  planes that intersect the turbines rotor disk). The wind-turbine rotors are denoted with vertical white lines while the vertical and horizontal black dashed lines indicate the starting location of the fringe region and the RDL

precursor domain. The flow direction at hub height remains quasi-parallel to the  $x$ -direction, with  $\langle \bar{\Phi} \rangle(z_h) = 0.15^\circ$ . The boundary layer growth is limited by the presence of the capping inversion which shows a constant height along the streamwise direction since no momentum sinks or sources are applied within the ABL (apart from the wall stress). This precursor simulation provides the inflow condition for the main domain, which is shown in Fig. 9b, d. In front of the farm, the wave-free fringe-region technique does not cause oscillations in the velocity magnitude. Instead, the velocity gradually decreases as a response to the gravity-wave induced unfavourable pressure gradient (see below). In the side view, we can observe the formation of an internal boundary layer which grows along the streamwise direction. However, its growth is limited by the presence of the capping inversion, which is displaced upward. Therefore, to satisfy mass conservation, the flow is redirected around the farm, as visible in Fig. 9b. For a more detailed discussion on the flow physics, we refer to Lanzilao and Meyers (2022).

Similarly to the inviscid-flow simulations, the upward displacement of the capping inversion caused by the farm-induced momentum sink triggers gravity waves, which are visible in Fig. 10. Here, the time- and space-averaged vertical velocity field obtained with the stdFR-RDL and newFR-RDL setups are shown. Also here, the standard fringe-region method perturbs the flow downstream by exciting spurious gravity waves with higher amplitudes than the ones triggered by the farm. Contrarily, the wave-free fringe-region technique traps the perturbation within the fringe region, without altering the physics in the domain of interest. Moreover, the combination of the wave-free fringe-region technique with the tuned RDL leads to a reflectivity of only 0.75%, which is an order of magnitude lower than what was observed in previous studies (Taylor and Sarkar, 2007; Wu and Porté-Agel, 2017; Allaerts and Meyers, 2017, 2018). Finally, we notice that in both cases the flow is pushed downward at the trailing edge of the farm (i.e  $x = 25$  km). This negative perturbation in the vertical velocity field excites a second train of gravity waves which is out of phase with respect to the one triggered at the leading edge (i.e  $x = 10$  km). Whether this phenomenon occurs or not depends on the gravity-wave vertical wavelength and the length and width of the farm. Its effects on wind-farm performances is an interesting topic for future research.

The internal gravity waves shown in Fig. 10 transport energy upward. This is illustrated in Fig. 11a, b, which displays a side view of the time- and space-averaged internal wave energy flux obtained with the standard and new fringe-region technique, respectively. Spurious gravity waves increase the amount of energy transported upward (red patches). Consequently, more energy is also reflected downward (blue patches). This gives rise to the checkerboard pattern visible in Fig. 11a. Contrarily, Fig. 11b shows that energy is primarily transported upward and along lines parallel to the wave-front, which is in agreement with gravity-wave theory (Nappo, 2002; Lin, 2007). Moreover, the dash-dotted green line, which represents the angle that the gravity-wave



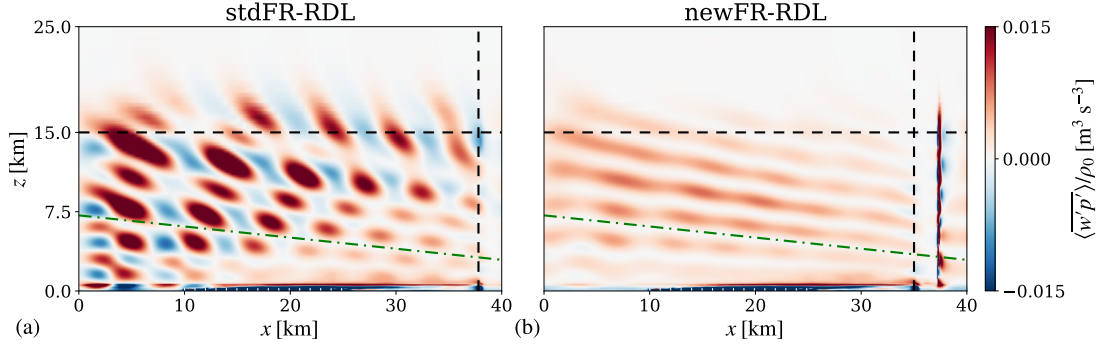


**Fig. 11** (a,b) Internal wave energy flux averaged over time and along  $x$ - $z$  planes within the turbine columns footprint obtained with the stdFR-RDL and newFR-RDL setups, respectively. The wind-turbine rotors are denoted with vertical white lines while the vertical and horizontal black dashed lines indicate the starting location of the fringe region and the RDL. Finally, the green dash-dotted line denotes the inclination of the gravity-wave phase line predicted by linear theory

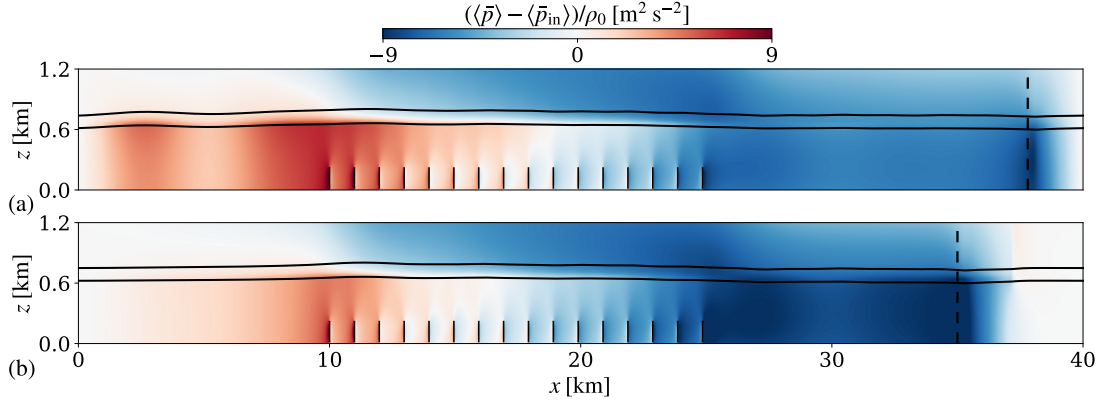


**Fig. 12** Contours of pressure perturbation with respect to the pressure measured at the inflow for cases (a) stdFR-RDL and (b) newFR-RDL, averaged over time and along  $x$ - $z$  planes within the turbine columns footprint. The black solid lines show the time-averaged evolution of the inversion-layer base and top while the wind-turbine rotors are denoted with vertical black lines. The vertical black dashed lines indicate the starting location of the fringe region

phase lines make with the horizontal calculated using linear theory, is parallel to the actual phase lines predicted by our LES solver.

The time- and space-averaged pressure perturbation within the first 1.2 km obtained with the stdFR-RDL and newFR-RDL setups are shown in Fig. 12a, b, respectively. A favourable and unfavourable pressure gradient in the induction region of the farm is observed in Fig. 12a, which in turn causes a flow slow-down and speed-up (not shown). This non-physical behaviour is provoked by the spurious gravity waves induced by the standard fringe forcing. In fact, the velocity decreases monotonically in the farm-induction region when the wave-free fringe-region technique is used (not shown). Moreover, the pressure build-up for the stdFR-RDL simulation at the first turbine row is roughly 35% higher than in the newFR-RDL case. The solid black lines in Fig. 12 denote the bottom and top of the capping inversion. The spurious gravity waves triggered by the standard fringe-region technique cause a vertical displacement of the capping inversion near the inflow which is comparable to the one caused by the wind farm (see Fig. 12a). As expected, local maxima in the pressure distribution correspond to local maxima of the inversion layer displacement, and vice versa.

Finally, Fig. 13 shows a comparison of total turbulent kinetic energy  $e$  and total shear stress magnitude  $\tau$  obtained using the standard and wave-free fringe-region technique. For the latter, we show two cases. The first one adopts a height-dependent damping function (i.e. Eq. 5) while

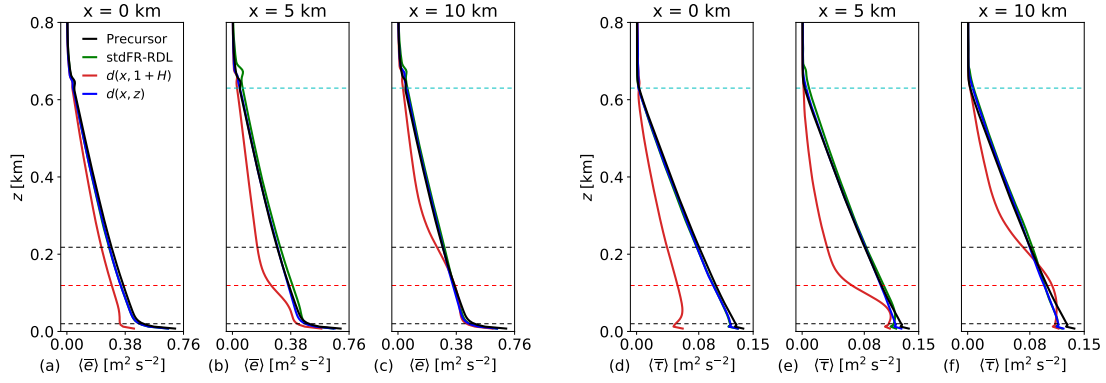


**Fig. 13** (a-c) Total (i.e. resolved and sub-grid scale contribution) turbulent kinetic energy  $e$  and (d-f) total shear stress magnitude  $\tau$  averaged over time and over the full spanwise direction obtained at the main-domain inflow ( $x = 0$  km),  $x = 5$  km and at the location of the first-row turbines ( $x = 10$  km). The green line represents the results obtained with the stdFR-RDL setup while the red and blue lines denote the results obtained with the newFR-RDL setups using a height-independent (i.e.  $d(x, 1 + H)$ ) and height-dependent (i.e.  $d(x, z)$ ) damping function, respectively. Moreover, the red dashed line denotes the hub height while the black dashed lines are representative of the rotor dimension. Finally, the light blue dashed line represents the boundary-layer height evaluated in the precursor domain

the second one uses  $d(x, 1 + H)$  which implies that the damping is also active inside the ABL (since  $\mathcal{H}(1) = 1$ ). It is evident from Fig. 13 that the latter case not only dampen spurious gravity waves but also turbulent fluctuations. In fact, both  $e$  and  $\tau$  are underestimated at the main-domain inflow (i.e.  $x = 0$  km). However, turbulence develops in the main domain so that the turbulence characteristics converge toward the precursor ones for increasing streamwise location. Contrarily, when the convective term in the vertical momentum equation is only dampened above the ABL, the turbulence characteristics observed at the main-domain inflow are comparable with the precursor ones. A similar behaviour is observed for the standard fringe-region technique. This suggests that, in case of a turbulent inflow profile, the wave-free fringe-region technique should adopt a  $x$ - and  $z$ -dependent damping function.

## 6 Conclusions

The aim of the current study was to develop a numerical setup which imposes the inflow and upper boundary conditions without distorting the numerical solution in LES of wind farms operating in stratified atmospheres. To this end, we implemented and compared two non-reflective upper boundary conditions, that is the RDL and the RC. Furthermore, we noticed that the standard fringe-region technique triggers spurious gravity waves. Therefore, we have developed a wave-free fringe-region technique which imposes the inflow condition while limiting spurious effects on the surrounding flow. We achieved this by locally damping the convective term in the vertical momentum equation. The different numerical setups have been tested in both inviscid- and viscid-flow environments.

We started our analysis with inviscid-flow simulations on a two-dimensional domain ( $x$ - $z$ ). First, we proposed a method to properly calibrate the Rayleigh function to minimize wave reflection together with the computational burden that comes with this additional sponge layer. Results showed that a tuned RDL can reduce the reflectivity of several percentage points if compared with simulations that do not have such a layer. Moreover, the RDL outperformed the RC in all cases analyzed. Next, we have shown that the standard fringe forcing triggers spurious gravity waves. The amplitude of such waves can be 3 to 4 times higher than the amplitude of gravity waves induced by the smooth box-like force term. This mainly causes an overestimation of the pressure build-up in front of the forcing region together with non-physical streamwise velocity oscillations. Conversely, the solution obtained with the wave-free fringe-region technique

closely follows the reference one. Good agreement with gravity-wave linear theory was also observed. Next, the different numerical setups have been applied to 169 atmospheric states and two different box-like forcing region lengths. Reflectivity values up to 80% were observed in subcritical flow conditions when the standard fringe-region technique was used. Moreover, in all cases, the new fringe-region technique outperformed the standard method, imposing the inflow conditions with a minimal impact on the surrounding flow. Overall, the tuned RDL in combination with the wave-free fringe-region technique (i.e. newFR-RDL) was the setup which provided the best performance, with reflectivity values below 1% in most of the cases.

Further, we extended the analysis to a three-dimensional domain, where the box-like forcing region emulated the momentum sink generated by a large wind farm. Also in this case, the newFR-RDL setup allowed us to impose the inflow condition without altering the flow fields downstream. Moreover, a good agreement between our numerical solutions and the theory of Smith (1980) was observed.

Finally, we have compared the performance of the standard and wave-free fringe-region techniques in an LES of a large wind farm operating in a CNBL. Despite the use of a turbulent inflow condition, we observed similar results. The standard fringe-region technique introduced spurious gravity waves in the domain of interest. These waves caused an oscillation in the pressure distribution, which led to a 30% higher pressure build-up in front of the farm when compared against the results obtained with the wave-free fringe-region method. In fact, in the latter case, the pressure and the streamwise velocity components showed monotonic trends in the farm induction region. We note that a reflectivity of only 0.75% was obtained with the newFR-RDL setup, which is an order of magnitude lower than what was observed in previous studies.

In light of these results, we conclude that a properly tuned Rayleigh function in combination with a wave-free fringe-region technique provide an effective framework for LES of wind farms that operates in stratified atmospheres. In the future, we are planning to adopt this numerical setup to further study gravity-wave effects on wind-farm operations.

**Acknowledgements** The authors acknowledge support from the Research Foundation Flanders (FWO, grant no. G0B1518N), and from the project FREEWIND, funded by the Energy Transition Fund of the Belgian Federal Public Service for Economy, SMEs, and Energy (FOD Economie, K.M.O., Middenstand en Energie). The computational resources and services in this work were provided by the VSC (Flemish Supercomputer Center), funded by the Research Foundation Flanders (FWO) and the Flemish Government department EWI.

**Data Availability** The datasets generated and/or analysed during the current study are available from the corresponding author on reasonable request.

## Appendix 1: Smooth Box-Like Force Model

In the inviscid-flow simulations, we use a smooth box-like force model which emulates the presence of a wind-farm, generating a momentum sink within the ABL. Such a force term is defined by the function

$$f_1(\mathbf{x}) = \beta \frac{U_\infty^2}{D_s} \frac{\mathcal{S}(x, L_x^s, \delta_x, x_0) \mathcal{S}(y, L_y^s, \delta_y, y_0) \mathcal{S}(z > 0, 2L_z^s, \delta_z, 0)}{s_c(L_x^s, \delta_x) s_c(L_y^s, \delta_y) s_c(L_z^s, \delta_z/2)} \quad (7)$$

where

$$\mathcal{S}(s, L, \delta, s_0) = \begin{cases} \cos(\pi[s - (s_0 - L/2 + \delta)/4\delta]), & \text{if } s_0 - L/2 - \delta < s < s_0 - L/2 + \delta \\ 1, & \text{if } s_0 - L/2 + \delta < s < s_0 + L/2 - \delta \\ \cos(\pi[s - (s_0 + L/2 - \delta)/4\delta]), & \text{if } s_0 + L/2 - \delta < s < s_0 + L/2 + \delta \\ 0, & \text{otherwise} \end{cases}$$

$$s_c(L, \delta) = L + 2\delta(4 - \pi)/\pi.$$

The parameters  $L_x^s + 2\delta_x$ ,  $L_y^s + 2\delta_y$  and  $L_z^s + \delta_z$  determine the size of the box-like forcing region, with  $\delta_x$ ,  $\delta_y$  and  $\delta_z$  controlling the smoothness of the profiles to minimize the role of



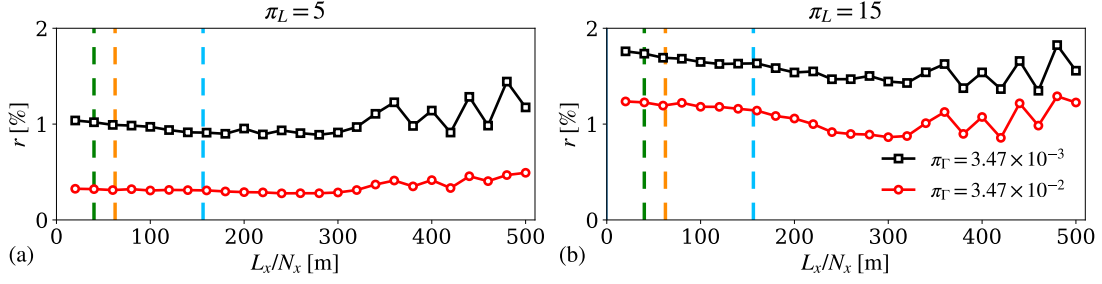


**Fig. 14** Grid sensitivity analysis for (a)  $\pi_L = 5$  and (b)  $\pi_L = 15$  performed with the newFR-RDL numerical setup (hence  $L_x = 40$  km). The light blue, orange and green vertical dashed lines refer to the grid resolution adopted in Sects. 3.1, 3.3 and 3.2, respectively

non-linear effects. Moreover, the scaling term  $s_c$  ensures that the integrated force over the whole computational domain equals to  $\beta U_\infty^2 / D_s$ , where  $U_\infty$  denotes the inflow velocity,  $D_s$  represents a length scale related to the turbine-rotor diameter while  $\beta$  is a non-dimensional parameter which regulates the magnitude of the force term. Following Allaerts (2016), we fix  $U_\infty = 12 \text{ m s}^{-1}$ ,  $D_s = 100 \text{ m}$  and  $\beta = 0.01$ . Finally, the centre of the forcing region along the  $x$ - and  $y$ -direction is denoted with  $x_0$  and  $y_0$ . Note that the momentum sink is applied only to the  $u$ -momentum equation, meaning that  $f_2(\mathbf{x}) = f_3(\mathbf{x}) = 0$ .

In the two-dimensional inviscid-flow simulations, the box-like forcing region starts at 100 km when the reference setup is used and at 10 km in the other cases. Here, we use two  $L_x^s$  values, that is 5 km and 15 km, with  $L_z^f = 0.6 \text{ km}$ . The smoothing parameters along the  $x$ - and  $z$ -direction are fixed to  $\delta_x = 0.5 \text{ km}$  and  $\delta_z = 0.4 \text{ km}$ . We note that  $H = L_z^s + \delta_z$ , meaning that the force is applied within the whole region below the capping inversion, similarly to Smith (2010, 2022). The same setup is used in the three-dimensional inviscid-flow simulations, with the difference that  $L_x^s = 15 \text{ km}$ ,  $L_y^s = 9 \text{ km}$  and  $\delta_y = 0.5 \text{ km}$ . Note that in the two-dimensional simulations we fix  $\mathcal{S}(y, L_y^s, \delta_y, y_0) = 1$  and  $s_c(L_y^s, \delta_y) = 1$ .

## Appendix 2: Grid Sensitivity Study

We perform a grid sensitivity analysis to determine the dependence of the reflectivity on the grid resolution in an inviscid-flow environment. To this end, we use the newFR-RDL setup described in Section 3.2 and we vary the grid resolution in the  $x$ -direction spanning from 500 m to 20 m with  $L_x = 40 \text{ km}$ . Results obtained with the atmospheric states adopted in Sect. 3.2 are shown in Fig. 14. When  $\pi_L = 5$  and  $\pi_\Gamma = 3.47 \times 10^{-2}$ , the reflectivity obtained on a grid with resolution of 156.25 m (used in Sect. 3.1) and 40 m (used in Sect. 3.2) is 0.32% and 0.31%, respectively. A similar difference is observed when a weaker free lapse rate is adopted (i.e  $\pi_\Gamma = 3.47 \times 10^{-3}$ ), although some oscillations in the  $r$  value take place at coarser grid resolutions. An analogous pattern is shown in Fig. 14b. These results suggest that the numerical solution is grid independent, justifying the changes in grid resolution made throughout Sects. 3 and 4.

## Appendix 3: Two-Dimensional Inviscid-Flow Simulations Computed on the Long Domain

In this appendix, we display the full-domain vertical velocity field obtained using the stdFR-RDL-LD and newFR-RDL-LD (also named as Reference) setups defined in Sect. 3.2. Figure 15 illustrates the vertical velocity obtained with different  $\pi_L$  and  $\pi_\Gamma$  values. With a domain length of 200 km, it is even more evident how the standard fringe-region technique triggers spurious gravity waves, perturbing the flow field downstream. With such a long domain, the perturbations

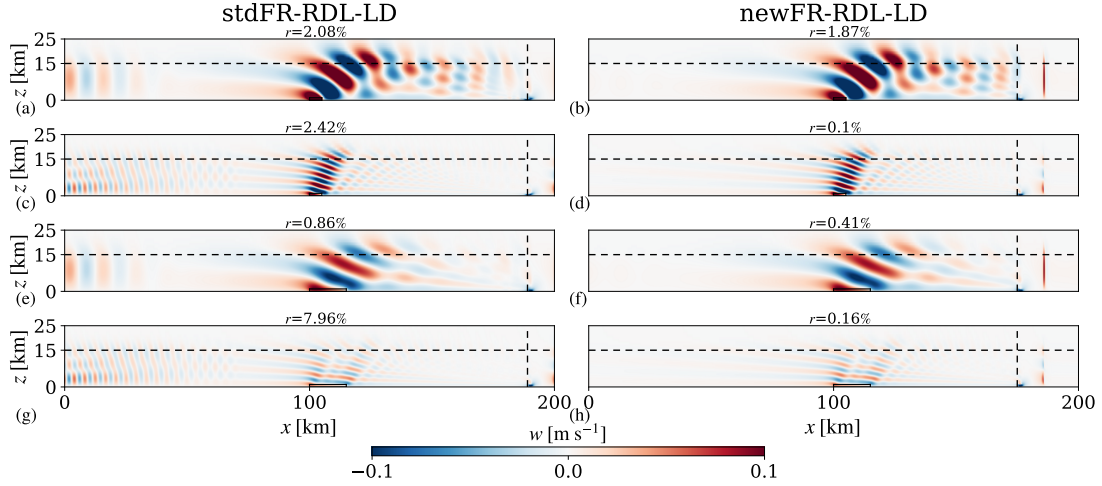


**Fig. 15** Side view of vertical velocity obtained with (a,b)  $\pi_L = 5$  and  $\pi_F = 3.47 \times 10^{-3}$ , (c,d)  $\pi_L = 5$  and  $\pi_F = 3.47 \times 10^{-2}$ , (e,f)  $\pi_L = 15$  and  $\pi_F = 3.47 \times 10^{-3}$  and (g,h)  $\pi_L = 15$  and  $\pi_F = 3.47 \times 10^{-2}$ . The snapshots display the full-domain reference solution obtained with the standard and wave-free fringe-region techniques. The black solid lines denote the region in which the box-like force term is applied. The black horizontal and vertical dashed lines indicate the starting location of the RDL and the fringe region

die out before reaching the box-like forcing region. Therefore, the phase lines of the gravity waves induced by the momentum sink are not distorted. Contrarily, the vertical velocity fields obtained with the wave-free fringe-region method do not alter the flow physics in the domain of interest. Moreover, Fig. 15b, d, f, h also shows that the domain length is large enough for the newFR-RDL-LD solution to be considered as the reference, since it is not affected by the boundary conditions. Finally, the wave-free fringe-region technique also reduces the reflectivity. For instance, we measure reflectivity values of 7.96% and 0.16% with the standard and wave-free fringe-region method, respectively, when  $\pi_L = 15$  and  $\pi_F = 3.47 \times 10^{-2}$  (see Fig. 15g, h).

## References

- Allaerts D (2016) Large-eddy simulation of wind farms in conventionally neutral and stable atmospheric boundary layers. PhD thesis
- Allaerts D, Meyers J (2015) Large eddy simulation of a large wind-turbine array in a conventionally neutral atmospheric boundary layer. *Physics of Fluids* 27(6):065,108, DOI 10.1063/1.4922339
- Allaerts D, Meyers J (2016) Effect of inversion-layer height and coriolis forces on developing wind-farm boundary layers. *AIAA SciTech* 6:521–538
- Allaerts D, Meyers J (2017) Boundary-layer development and gravity waves in conventionally neutral wind farms. *J Fluid Mech* 814:95–130
- Allaerts D, Meyers J (2018) Gravity waves and wind-farm efficiency in neutral and stable conditions. *Boundary-Layer Meteorol* 166:269–299
- Allaerts D, Meyers J (2019) Sensitivity and feedback of wind-farm induced gravity waves. *J Fluid Mech* 862:990 – 1028
- Bennett AF (1976) Open boundary conditions for dispersive waves. *J Atmos Sci* 33:176–182
- Bortolotti P, Tarrés HC, Dykes K, Merz K, Sethuraman L, Verelst D, Zahle F (2019) Iea wind task 37 on systems engineering in wind energy wp2.1 reference wind turbines. Technical report
- Bougeault P (1982) A non-reflective upper boundary condition for limited-height hydrostatic models. *Monthly Weather Review* 111:420–429
- Béland M, Warn T (1975) The radiation condition for transient rossby waves. *J Atmos Sci* 32:1873–1880

- Calaf M, Meneveau C, Meyers J (2010) Large eddy simulation study of fully developed wind-turbine array boundary layers. *Phys Fluids* 22:015,110
- Devesse K, Lanzilao L, Jamaer S, van Lipzig N, Meyers J (2022) Extending the applicability of a wind-farm gravity-wave model to vertically non-uniform atmospheres. *Wind Energy Science Discussions* 2022:1–25, DOI 10.5194/wes-2021-138
- Dhamankar NS, Blaisdell GA, Lyrantzis AS (2015) Overview of turbulent inflow boundary conditions for large-eddy simulations. *Aiaa Journal* 56(4):1317–1334
- Doyle JD, Shapiro MA, Jiang Q, Bartels DL (2005) Large-amplitude mountain wave breaking over greenland. *J Atmos Sci* 62:3106–3126
- Durran DR, Klemp JB (1983) A compressible model for the simulation of moist mountain waves. *Mon Wea Rev* 111:2341–2361
- Gadde SN, Stevens RJAM (2021) Interaction between low-level jets and wind farms in a stable atmospheric boundary layer. *Phys Rev Fluids* 6:014,603, DOI 10.1103/PhysRevFluids.6.014603
- Gill AE (1982) *Atmosphere-ocean dynamics*. International Geophysics Series 30:Academic Press, San Diego, USA
- Goit JP, Meyers J (2015) Optimal control of energy extraction in wind-farm boundary layers. *J Fluid Mech* 768:5–50
- Hu FQ (2008) Development of pml absorbing boundary conditions for computational aeroacoustics: A progress review. *Computers and Fluids* 37:336–348
- Hu FQ, Li XD, Lin DK (2008) Absorbing boundary conditions for nonlinear euler and navier–stokes equations based on the perfectly matched layer technique. *Journal of Computational Physics* 227:4398–4424
- Inoue M, Matheou G, Teixeira J (2014) Les of a spatially developing atmospheric boundary layer: Application of a fringe method for the stratocumulus to shallow cumulus cloud transition. *Monthly Weather Review* 142:1365–1393
- Jiang Q, Doyle JD (2004) Gravity wave breaking over the central alps: Role of complex terrain. *J Atmos Sci* 61:2249–2266
- Klemp JB, Durran DR (1982) An upper boundary condition permitting internal gravity wave radiation in numerical mesoscale models. *Monthly Weather Review* 111:430–444
- Klemp JB, Lilly DK (1977) Numerical simulations of hydrostatic mountain waves. *Journal of the atmospheric sciences* 35:78–107
- Klemp JB, Dudhia J, Hassiotis AD (2018) An upper gravity-wave absorbing layer for nwp applications. *Monthly Weather Review* 136:3987–4004
- Lanzilao L, Meyers J (2021) Set-point optimization in wind farms to mitigate effects of flow blockage induced by atmospheric gravity waves. *Wind Energy Science* 6(1):247–271
- Lanzilao L, Meyers J (2022) Effects of self-induced gravity waves on finite wind-farm operations using a large-eddy simulation framework. *Journal of Physics: Conference Series* 2265(2):022,043, DOI 10.1088/1742-6596/2265/2/022043
- Lin YL (2007) *Mesoscale Dynamics*. Cambridge University Press, DOI 10.1017/CBO9780511619649
- Lundbladh A, Berlin S, Skote M, Hildings C, Choi J, Kim J, Henningson DS (1999) An efficient spectral method for a simulation of incompressible flow over a flat plate. *Trita-mek Tech Rep: 11 KTH*
- Maas O, Raasch S (2022) Wake properties and power output of very large wind farms for different meteorological conditions and turbine spacings: a large-eddy simulation case study for the german bight. *Wind Energy Science* 7(2):715–739, DOI 10.5194/wes-7-715-2022
- Mason PJ, Thomson DJ (1992) Stochastic backscatter in large-eddy simulations of boundary layers. *Journal of Fluid Mechanics* 242:51–78, DOI 10.1017/S0022112092002271
- Moeng CH (1984) A large-eddy-simulation model for the study of the planetary boundary-layer turbulence. *Journal of the atmospheric science* 41:2052–2062
- Munters W, Meyers J (2018) Dynamic strategies for yaw and induction control of wind farms based on large-eddy simulation and optimization. *Energies* 11:177

- Munters W, Meneveau C, Meyers J (2016a) Shifted periodic boundary conditions for simulations of wall-bounded turbulent flows. *Physics of Fluids* 28(2):025,112, DOI 10.1063/1.4941912
- Munters W, Meneveau C, Meyers J (2016b) Turbulent inflow precursor method with time-varying direction for large-eddy simulations and applications to wind farms. *Boundary-layer meteorology* 159(2):305–328
- Nappo CJ (2002) An introduction to atmospheric gravity waves. *International Geophysics Series* 85:Academic Press, Waltham, USA
- Nordstrom J, Nordin N, Henningson D (1999) The fringe region technique and the fourier method used in the direct numerical simulation of spatially evolving viscous flows. *SIAM J Sci Comput* 20:1365–1393
- Parrish SA, Hu FQ (2009) Pml absorbing boundary conditions for the linearized and nonlinear euler equations in the case of oblique mean flow. *Int J Numer Meth Fluids* 60:565–589
- Porté-Agel F, Bastankhah M, Shamsoddin S (2020) Wind-turbine and wind-farm flows: A review. *Boundary-Layer Meteorol* 174:1–59
- Powers JG, Klemp JB, Skamarock WC, Davis CA, Dudhia J (2017) The weather research and forecasting model: overview, system efforts, and future directions. *Bulletin of the American Meteorological Society* 98
- Rampanelli G, Zardi D (2004) A method to determine the capping inversion of the convective boundary layer. *J Appl Meteor* 43:925–933
- Schlatter P, Adams N, Kleiser L (2005) A windowing method for periodic inflow/outflow boundary treatment of non-periodic flows. *Journal of Computational Physics* 206:505–535
- Smedman A, Bergstrom H, Grisogono B (1997) Evolution of stable internal boundary layers over a cold sea. *Journal of Geophysical Research* 102:1091–1099
- Smith RB (1980) Linear theory of stratified hydrostatic flow past an isolated mountain. *Tellus* 32:348–364
- Smith RB (2010) Gravity wave effects on wind farm efficiency. *Wind Energy* 13:449–458
- Smith RB (2022) A linear theory of wind farm efficiency and interaction. *Journal of the Atmospheric Sciences* DOI 10.1175/JAS-D-22-0009.1
- Spalart PR, Watmuff JH (1993) Experimental and numerical study of a turbulent boundary layer with pressure gradients. *J Fluid Mech* 249:337–371
- Stevens B, Moeng CH, Sullivan PP (2000) Entrainment and subgrid length scales in large-eddy simulations of atmospheric boundary-layer flows. *Symposium on Developments in Geophysical Turbulence* 58:253–269
- Stevens RJAM, Graham J, Meneveau C (2014) A concurrent precursor inflow method for large eddy simulations and applications to finite length wind farms. *Renewable Energy* 68:46–50
- Stieren A, Gadde SN, Stevens RJAM (2021) Modeling dynamic wind direction changes in large eddy simulations of wind farms. *Renewable Energy* 170:1342–1352
- Sutherland BR (2010) *Internal gravity waves*. Cambridge University Press
- Taylor JR, Sarkar S (2007) Internal gravity waves generated by a turbulent bottom ekman layer. *J Fluid Mech* 590:331–354
- Taylor JR, Sarkar S (2008) Direct and large eddy simulations of a bottom ekman layer under an external stratification. *Int J Heat Fluid Flow* 29:721–732
- Teixeira MAC (2014) The physics of orographic gravity wave drag. *Frontier in Physics* 2
- Verstappen RWCP, Veldman AEP (2003) Symmetry-preserving discretization of turbulent flow. *Journal of Computational Physics* 187:343–368
- Wu KL, Porté-Agel F (2017) Flow adjustment inside and around large finite-size wind farms. *Energies* 10:2164
- Zilitinkevich SS (1989) Velocity profiles, the resistance law and the dissipation rate of mean flow kinetic energy in a neutrally and stably stratified planetary boundary layer. *Boundary-Layer Meteorol* 46:367–387